

1 Double surface rupture and hydraulic recharge of a three-fault  
2 system during the Mw 4.9 earthquake of 11 November 2019 at Le  
3 Teil (France)

4

5 André Burnol<sup>1\*</sup>, Antoine Armandine Les Landes<sup>1</sup>, Daniel Raucoules<sup>1</sup>,  
6 Michael Foumelis<sup>1,2</sup>, Cécile Allanic<sup>1</sup>, Fabien Paquet<sup>1</sup>, Julie Maury<sup>1</sup>, Hideo  
7 Aochi<sup>1</sup>, Théophile Guillon<sup>1</sup>, Mickael Delatre<sup>1</sup>, Pascal Dominique<sup>1</sup>, Adnand  
8 Bitri<sup>1</sup>, Simon Lopez<sup>1</sup>, Philippe P. Pébay<sup>3</sup>, Behrooz Bazargan-Sabet<sup>1</sup>

9 *1. BRGM, 3 avenue Claude Guillemin, BP 36009, 45000 Orléans, France*

10 *2. Aristotle University of Thessaloniki (AUTH), School of Geology, Thessaloniki*

11 *3. Eredio, 28 rue de la Plane, 84330 Le Barroux*

12

13 \*Corresponding Author.

14 Email: [a.burnol@brgm.fr](mailto:a.burnol@brgm.fr)

15

16

**This manuscript is a non-peer reviewed preprint submitted  
to EarthArXiv and to Communications Earth & Environment.  
Please feel free to contact the corresponding author  
[a.burnol@brgm.fr](mailto:a.burnol@brgm.fr) ; we welcome feedback**

## 17        **Abstract**

18

19        The Mw 4.9 earthquake of 11 November 2019 at Le Teil (France) occurred at a  
20        very shallow depth (about 1 km) inducing the surface rupture of La Rouvière fault,  
21        nearby of a limestone quarry. Thanks to satellite differential interferometry, we  
22        detected the existence of the secondary surface rupture of the quasi-parallel Bayne  
23        Rocherenard fault. A newly processed seismic cross-section allowed us to construct  
24        a local 3D fault system. Assuming that the earthquake was triggered by the  
25        transient increase in hydraulic pressure following heavy rainfall before the event,  
26        our numerical 3D simulations demonstrate that the hydraulic pressure gradient is  
27        maximum just before the earthquake at the intersection of the two faults, the most  
28        probable place of the hypocenter. This hydraulic effect is about two and a half  
29        times larger than the cumulative effect of mechanical stress release due to the  
30        mass removal from the surface quarry over the two past centuries.

31

32

## 33        **1. Introduction**

34        Large earthquakes usually occur along preexisting faults and plate  
35        interfaces. However, intraplate earthquakes are difficult to assess, as many  
36        damaging earthquakes are not associated to the known major faults, which were  
37        considered as the highest seismic potential in the area<sup>1</sup>. Because the recurrence  
38        time of intraplate events is long, our knowledge and understanding of the fault  
39        dynamics (structure, rheology, stress loading and interaction) are still limited and  
40        causes other than the long-term tectonic stress loading are therefore considered  
41        for some earthquakes. For example, the 2008 Mw 7.9 Wenchuan (China)  
42        earthquake has a total fault length of more than 200 km in Longmenshan fault  
43        zone. Before the occurrence of the earthquake, the highest seismic potential of  
44        the area had never been attributed to the ruptured faults (causal faults) from the  
45        seismic hazard assessment<sup>2</sup> view point. Although the tectonic stress loading is  
46        undoubtable over the whole area, the nucleation process of this mega earthquake  
47        has been discussed in relation to the near-by Zipingpu reservoir in terms of the

48 elastic stress change and pore pressure change<sup>3-8</sup>. Indeed, any positive  
49 perturbation of stress on a causal fault can be suspected in triggering an  
50 earthquake<sup>9</sup>. The lack of *in situ* measurements does not allow however any  
51 definitive conclusion; the impoundment of the reservoir may have activated the  
52 shallow micro-seismicity within a few kilometers below the dam<sup>5,6</sup> but the link to  
53 the hypocenter of the earthquake more than 10 km away is not clear.

54 The anthropogenic influence on earthquake triggering has been widely studied and  
55 several authors produced overview of the likely cases<sup>10-15</sup>, covering a range of  
56 magnitude between 1 and 8. At a local scale, the microseismicity at Gardanne,  
57 southern France is correlated to the flooding of the underground abandoned mining  
58 gallery with a time lag of about ten days<sup>16</sup>. The driving mechanism behind  
59 triggering is not only human-driven but can also be related to natural variations  
60 on the Earth's surface, namely climate variations<sup>17-19</sup>. It is reported that the  
61 seismicity in Himalaya has a seasonal trend according to the annual monsoon  
62 season, namely large amounts of precipitation in the summer<sup>20,21</sup>. Among the  
63 studies analyzing the rainfall effect, the seasonal pore pressure evolution was  
64 discussed through fluid diffusion in the limestone of southeastern Germany<sup>19</sup>. The  
65 seismicity triggered by rainfall in karstic domain, in Switzerland, was studied  
66 through a fluid diffusion model in poro-elastic context<sup>22</sup>. The hypothesis of  
67 "hydroseismicity" developed by John K. Costain<sup>23-26</sup> attributes most intraplate and  
68 near-intraplate earthquakes to the dynamics of the hydrologic cycle. Such  
69 hydraulic perturbations may occur from a few kilometers to 10 km away if a  
70 permeably connected fault system exists. In France, a correlation between heavy  
71 rainfall and small earthquakes was shown in the Western Provence around the  
72 Nîmes Fault<sup>27</sup> and in the Provence Alps at Castellane<sup>28</sup>.

73 The 2019 Mw4.9 Le Teil (France) earthquake heavily damaged nearby

74 areas<sup>29</sup>. Regardless of its moderate magnitude, this earthquake ruptured the  
75 shallowest part of the known fault (only the first 2 km depth at most) and showed  
76 rupture traces on the ground surface (Figure 1). The area had been known with  
77 some historical earthquakes; however, earthquakes of this magnitude with surface  
78 ruptures had never been taken into account in local/regional seismic hazard  
79 assessment<sup>30,31</sup>. As a first analysis, some authors pointed out that a nearby  
80 limestone quarry may have contributed to the stress loading on the causal fault<sup>32-</sup>  
81 <sup>34</sup>. Using the seismograms available from the mainshock and aftershocks, Delouis  
82 *et al.* (2021) shows that the best inferred epicenter is probably located not inside  
83 but rather southwest of the surface quarry<sup>35</sup>. Conversely, we investigate in this  
84 work the so-called "hydraulic triggering hypothesis". Indeed, the studied area  
85 suffered heavy rainfall during the month before the seismic event. Therefore, a  
86 permeably connected fault system may play a role of conducting the pore pressure  
87 change at depth. We focus on the local hydraulic system in the study area derived  
88 from an updated regional geological model. The movement of moisture in partially-  
89 saturated media is simulated using a 3D diphasic flow double permeability model  
90 with the soil moisture data recorded during the period 2010-2019 as surface  
91 boundary and the Rhône river as edge boundary conditions. We then discuss the  
92 possible triggering mechanism by comparing the results of the hydraulic model  
93 with those of a 3D mechanical model that simulates the mass withdrawal due to  
94 the quarry exploitation in a similar geological configuration. We try to answer two  
95 essential questions: (1) How large is the hydraulic overpressure due to the  
96 meteoric water recharge vs. the Coulomb stress change due to the mass  
97 withdrawal from the surface quarry? (2) Is the estimated location of the maximum  
98 hydraulic overpressure consistent with the estimated hypocenter location?

99

## 100 2. Results

### 101 2.1. Geological and hydraulic context around the fault system

102 First, we collect the prior information on the fault system around Le Teil,  
103 independently of its co-seismic rupture process. The concerned area is located in  
104 the Rhône Valley in Southeastern France near the Montélimar city. The Urgonian  
105 limestones that are extracted from the nearby quarry were deposited in the early  
106 cretaceous epoch, during the Upper Barremian–Lower Aptian age and, afterwards,  
107 some calcareous marlstones are deposited during the Aptian–Albian age, east of  
108 La Rouvière Fault (LRF) (Figure 1). The available geological map<sup>36</sup> of the studied  
109 area at a scale of 1:50 000 shows the existence of several, mostly NE-SW striking  
110 fault segments in the area. The observed surface rupture<sup>30</sup> is consistent with the  
111 portion of the already mapped La Rouvière fault (LRF). The geometry of each  
112 segment of the geological map is studied through the differential SAR  
113 interferometry (DInSAR) analysis using the available Sentinel-1 images. The  
114 interpretation of seismic cross section is presented in the next section.

115 The hydraulic parameters in the Barremian limestones are highly variable.  
116 The continuous medium (“matrix”) and the “fault” elements are characterized by  
117 a large range of porosity and permeability<sup>37,38</sup> (Table 1). For the “matrix”, we use  
118 a permeability of  $10^{-16}$  m<sup>2</sup> and a porosity of 20% corresponding to the average  
119 values measured in the Low Noise Underground Laboratory (LSBB)  
120 (<https://lsbb.cnrs.fr/>) in the host rock of Upper Barremian limestones (Urgonian  
121 facies)<sup>37</sup>. For the “fault”, a homogeneous high fault permeability value of  $10^{-11}$  m<sup>2</sup>  
122 (i.e. a hydraulic conductivity of  $k \sim 10^{-4}$  m s<sup>-1</sup> at 500 m depth) and a mean fault  
123 porosity of 10% are chosen to explore the infiltration in a highly conductive,  
124 intensively fractured fault zone that is representative of fast fluid conduits in the  
125 shallow subsurface. Such high permeability values are expected in the porous

126 layers along the fault zones in the Upper Barremian/Urgonian limestones<sup>38-40</sup>.  
127 These hydraulic parameters are used in the reference simulations of our 3D double  
128 porosity double permeability model (Table 1).

129

## 130 2.2. Surface traces of the fault system using DInSAR

131 Spaceborne Differential SAR interferometry (DInSAR) has been widely used  
132 during the past decades to track land subsidence or uplift related to groundwater  
133 extraction or underground gas storage<sup>41</sup>. The same method has been also  
134 successfully used for identifying ruptures due to earthquakes and quantifying the  
135 co-seismic motion<sup>42,43</sup>. We particularly aim to refine the location of ruptures with  
136 a particular interest on La Rouvière fault (LRF) and the surrounding ones mapped  
137 on the 1:50 000 geological maps<sup>36</sup>. To carry out this analysis, four interferograms  
138 were produced using SAR data from the Sentinel-1 mission (Method section and  
139 Figures S1-S4). After visual analysis of the four produced interferograms set (Table  
140 S1), only track A059 has sufficient quality on the area of major deformation. The  
141 interpretation of this interferogram is shown in Figure 2. The final geocoded  
142 product has 15 m spatial sampling. While the main rupture along LRF is clearly  
143 identified on the A059 interferogram, a secondary rupture can be suspected from  
144 the pattern of the deformation at the extremities of the ruptured area (Figure 2c  
145 and 2d). This latter coincides mostly with the mapped Bayne Rocherenard Fault  
146 (BRF) in the south-western area of the studied area, and this continues in the  
147 north-eastern direction, always parallel to the LRF, after the intersection with the  
148 Paurière Fault (PF) (Figure 2e). The interferometric coherence is better on the  
149 south-western part of the BRF than on its north-eastern part (more black pixels in  
150 Figure 2e). Figure 3 compares the identified positions with the cartographic  
151 representation of the faults as well as the differential motion along the rupture

152 traces. The main rupture along LRF exhibits motion up to 14 cm in Line of Sight  
153 (LOS) in the central part of the rupture (points LRF5 to LRF14 between 1000-  
154 3000m), that is consistent with previous results<sup>30</sup>. The differential motion along  
155 BRF is estimated up to 4 cm, about one third of the main motion along LRF (Figure  
156 3). The south-western part along BRF (BRR1 to BRR10 between 2000-3800m  
157 distance) moved two times less (about 2 cm) than the north-eastern part (BRR11  
158 to P8 between 3900-5400m). The LRF motion moved more on the central part of  
159 the rupture (points LRF5 to LRF14 between 1000-3000m). This interferogram  
160 interpretation suggests the re-positioning of the north-eastern part of BRF. Most  
161 of the surface rupture evidences documented in the field<sup>30</sup> are close to LRF on the  
162 geological map<sup>36</sup>, but one of them is found near the point P7 along the fault trace  
163 in Figure 3a, consistent with our proposed north-eastern extension of BRF. To be  
164 consistent with DInSAR analysis, we need therefore to reconstruct the fault model  
165 in the area: the found trace of BRF does not intersect with LRF on the ground  
166 surface, and this fault remains secondary in terms of the differential displacement.  
167 The 3D geometry is presented in the next section using a newly processed seismic  
168 cross-section.

169

### 170 2.3. 3D geometry of the fault system using M201 cross-section

171 In order to clarify the possible connectivity of the two faults (LRF and BRF), we  
172 re-interpret the seismic cross-section (M201, available on [www.minergies.fr](http://www.minergies.fr)),  
173 whose location is shown in Figures 1 and 3. This profile was acquired by CGG  
174 company during 1962-1963 and retreated in 2020 by BRGM after Le Teil  
175 earthquake. Our seismic interpretation<sup>44</sup> of the geological layers in Figure 4 is  
176 partly based on the Valvignères exploration well drilled in 1963 (BSS002ARWX well  
177 at <http://infoterre.brgm.fr/>, see location in Figure S6). Since our work aims to

178 study the hydraulic and mechanical influence from the ground surface, we only  
179 focus on the local shallow structure of the first 2 km depth and follow from west  
180 to east La Rouvière (LRF), Bayne Rocherenard (BRF) and Paurière (PF) faults  
181 (Figure 5). LRF is a south-east dipping fault, consistent with the focal mechanism  
182 and finite source inversions of Le Teil earthquake<sup>32,35</sup>. The seismic cross-section  
183 indicates that BRF is branching from LRF and PF is branching further from BRF.  
184 The position of each fault on the ground surface allowed us to estimate the dip  
185 angles, supposing that the dip angles are approximatively constant (see Texts S1-  
186 3 in Supplementary Information). We found a true dip angle of 54° for LR and this  
187 value between 45° and 60° is consistent with previous works<sup>30</sup>. This shapes the  
188 geometry of our model at a local scale. This model is derived from an updated 3D  
189 geological model at a regional-scale<sup>44</sup> (up to 100 km horizontally and down to 5  
190 km depth).

191 The SC03 borehole drilled by the quarry owner near the point P0 of the new  
192 BRF trace (Figure 3a) provides us some additional evidences that support this 3D  
193 fault model. The SC03 core samples show indeed at 90.5 m depth a near-vertical  
194 natural fracture with calcite veins (Figure S5) and at 112.5 m depth the geological  
195 evidence for fluids overpressures with angular fragments organized in a jigsaw  
196 puzzle pattern. Both observations indicate a possible intersection of SC03 with the  
197 new north-eastern part of BRF (Supporting Information, see Text S3). Another  
198 interesting observation is that an important quantity of water was lost at 83 m  
199 depth during the SC03 geotechnical drilling in 2016 inside the Le Teil quarry  
200 perimeter (personal communication of the quarry owner LAFARGE CEMENTS). We  
201 infer that the BRF fault zone could form a drain along the fracture network leading  
202 to fault parallel flows.

203

## 204 2.4. Hydraulic simulations using ComPASS

205  
206 The precipitation data are compared with the seismic events during the  
207 period 2010-2019 in a rectangular area of 50 km x 25 km around the Teil quarry  
208 (Figure S6). Seismic data are extracted from the French national RéNaSS  
209 catalogue and the rainfall is measured by the weather station at Montélimar  
210 (44.58°N, 4.74°E) (Figure S6). The three most intense rainfalls between 2010 and  
211 2019 (4<sup>th</sup> May 2010, 4<sup>th</sup> November 2014, 24<sup>th</sup> October 2019) are followed by a  
212 seismic event in this restricted area, which occurs between 8 and 18 days after  
213 these rainy episodes (Figure S6). The same delay was observed in other studies  
214 within a similar carbonate geological context<sup>19,28</sup>. However, the number of events  
215 in this comparison is quite limited (only 12) and a statistical analysis is therefore  
216 not possible. Using our re-constructed fault model, we estimate here the pressure  
217 variations at depth linked to the infiltration of meteoric water in the period  
218 preceding the earthquake of 11 November 2019. In order to exclude as much as  
219 possible the evapotranspiration and surface runoff contributions, we use the soil  
220 moisture data at 30 cm (SM30) instead of the rainfall data during the period 2015-  
221 2019 (Figure 6). In order to simulate the previous period between 2010 and 2015,  
222 we use also the surface soil moisture (SSM) data acquired by the SMOS satellite  
223 (Figures 6 and S6). These data (SM30 or SSM) are used as input for the nodes at  
224 the top surface of the domain, except for those that belongs to the Rhône river  
225 where a constant/fixed boundary condition is applied (see Method section). Figure  
226 5 illustrates the model volume consisting of the reconstructed fault model including  
227 the three-fault system (LRF, BRF and PF) as well as two other dipping faults close  
228 to the Rhône River. We adopt a so-called hybrid dimensional model coupling a 3D  
229 model of the matrix with a 2D model in fault planes using ComPASS<sup>45,46</sup> (Method  
230 section).

231 In the reference case noted Ref16, we assume a permeability of  $10^{-18} \text{ m}^2$  in the  
232 surface Apto-Albian clayey layer (Figure 5b), that is about 100 times lower than  
233 Upper Barremian limestones layer due to the clay fraction (Table 1). Soil moisture  
234 data at 30 cm depth (SM30) are used over the period 2015-2019 (Figure 6). The  
235 date of 24<sup>th</sup> September 2019 corresponds to a relative minimum pressure during  
236 the period 2015-2019 (Figure 7d-e). The differential of pressure ( $\Delta P$ ) for the period  
237 preceding the earthquake (between 24<sup>th</sup> September 2019 and 11<sup>th</sup> November  
238 2019) is shown in Figure 7a-b. A peak value of  $\Delta P$  appears along the intersection  
239 line between BRF and LRF (Figure 7c) which is higher than the peak value along  
240 the intersection line between PF and LRF (Figure 7a).  $\Delta P$  reaches the maximum  
241 value of 0.98 MPa (982 kPa or 9.8 bars) at  $Y = 1963 \text{ m}$  (Figure 7c) near the  
242 junction of the three-fault system LRF, BRF and PF. The temporal evolution of the  
243 pressure at this node is shown in Figure 7d between Mai 2015 and December 2019,  
244 revealing that the pressure gradient is maximum during the period just before the  
245 earthquake of November 11, 2019 (red dot). Using the 10-day SSM products for  
246 descending overpasses starting from 2010, we demonstrate that this pressure  
247 gradient is also maximum just before the earthquake during all the decade 2010-  
248 2019 (Figure S6). Therefore, a maximum overpressure on LRF takes place near  
249 the junction of the three faults at around 1,200 m depth. We verify here that the  
250 intersections between two or multiple faults are the most probable location zones  
251 for the hypocenter of an earthquake triggered by a hydraulic recharge according  
252 to the "hydroseismicity" concept developed by Costein<sup>25</sup>.

253 The simulation results are qualitatively stable since the surface moisture is  
254 transported principally by BRF to the depth and the peak of the pore pressure  
255 appears around the junction of the three faults. Another case called Ref20  
256 corresponds to a simplified scenario with a homogeneous permeability of  $10^{-16} \text{ m}^2$

257 in the matrix (Table 1). In that case, we obtain a differential pressure of about  
258 0.975 MPa. This counterintuitively indicates that the surface clays does not play a  
259 predominant role in establishing the hydraulic overpressure on LRF at depth. If we  
260 use SSM instead of SM30, the maximum differential of pressure decreases to the  
261 value of 0.9 MPa (Table 1). This slight decrease of the simulated overpressure is  
262 consistent with the observation that the SMOS-CATDS products underestimate  
263 generally the *in situ* soil moisture at Berzème (Figure 6), as already reported in  
264 southern France by others<sup>47</sup> (average bias of -9.5 vol.%).

265

### 266 3. Discussion

267

268

Our simulations show that the pore pressure change may reach 0.98 MPa at  
269 a depth of around 1.2 km at the intersection of LRF and BRF. It is thus naturally  
270 questioned how this is significant comparing to the mechanical impact due to the  
271 mass removal at Le Teil historical quarry nearby. Prior analytical evaluation of  
272 Coulomb stress, based on Boussinesq solution in a homogeneous half-space elastic  
273 medium show variations of 0.15 to 0.2 MPa<sup>32,48</sup>. It is important to note that the  
274 earlier amplitude value of about 1 MPa proposed by De Novellis et al. (2020) was  
275 later corrected<sup>48</sup>. We perform new 3D numerical simulations using 3DEC<sup>TM</sup> distinct-  
276 element code<sup>49</sup> to represent our improved geological model including  
277 discontinuities as well as lithology in a 3D medium. The spatial distributions of  $\Delta\sigma_n$   
278 and  $\Delta\tau$  on LRF are shown in Figure 8c and Figure 8d, respectively (Method section).  
279 The variations of the Coulomb Failure Function ( $\Delta CFF$ ) show a maximum change  
280 of 0.25 MPa at around 1 km depth on LRF (Figure 8b), a value of the same order  
281 as the Boussinesq solution<sup>32,48</sup>. When we look carefully at the LRF, one peak (0.25  
282 MPa) exists above the intersection with BRF, while another peak (0.24 MPa)  
283 appears along the intersection of LRF and BRF, promoted by the plasticity of the

284 fault element. An important portion of shear stress on LRF is generated along the  
285 fault line between LRF and BRF (Figure 8d). The Coulomb stress change  $\Delta CFF$  is  
286 simulated by 3DEC<sup>TM</sup> on all the considered fault segments (Figure S7). The  
287 maximum value of  $\Delta CFF$  among all the faults appears not on LRF but on BRF (0.39  
288 MPa at maximum). It is worthy to note that the mechanical stress change can be  
289 larger around the intersection of LRF and BRF and that BRF is more favorably  
290 located than LRF in terms of the mechanical stress change. The Coulomb stress  
291 change  $\Delta CFF = |\Delta\tau| - \mu\Delta\sigma_n$  should be compared to the hydraulic term  $\mu\Delta P$  with  $\Delta P$   
292 of about 1 MPa and  $\mu$  of 0.6 (Method section). The study highlights that the  
293 hydraulic term  $\mu\Delta P$  (0.6 MPa) is about two and a half times larger than the  
294 mechanical stress change (0.24 MPa) due to the mass removal from the ground  
295 surface. Moreover, the mechanical unloading remains a long-term quasi-static  
296 process over nearly 200 years while the hydraulic effect is a dynamic process  
297 immediately preceding the earthquake nucleation.

298 Another important discussion point is the consistency of the multiple  
299 relocation approaches of the hypocenter location. The studied area had not been  
300 covered by a dense seismic network before the earthquake. The closest station of  
301 the permanent network is far from the source area by about 30 km (OGLP station  
302 in Résif; <https://seismology.resif.fr/>), thus the hypocenter location using any  
303 catalogue has a significant uncertainty of several km<sup>31</sup>. However, a local network  
304 was installed just after the seismic event and the hypocenter of the Le Teil  
305 earthquake has been recently relocated using multiple approaches<sup>35</sup> (e.g.  
306 calibration from aftershocks). The most probable hypocenter location is at  
307 (44.5188 N, 4.6694 E, and 1.3 km depth) with an error of about 500m. This  
308 epicenter position is very close to the surface projection of the intersection of LRF  
309 and BRF (Figures 8 and 9). It is also close to the projected locations of the

310 maximum overpressures of both Ref16 and Ref20 reference simulations. A near-  
311 by blast monitoring station CLAU recorded the mainshock (Figure 9). Although this  
312 short period sensor was *a priori* only calibrated for micro-vibrations of quarry  
313 blasts, we found that the first particle motion could bring some useful information  
314 after testing one known blast event (Method section and Figure S9). The azimuth  
315 and its associated uncertainty of the first wave arrival of the mainshock is  
316 estimated to N164°E  $\pm$ 16° (Figure 9). This direction is also consistent with our  
317 suggested epicenter locations. Observing this accordance between the  
318 seismological analyses and our hydraulic- and mechanical- modeling, we suggest  
319 that the intersection of LRF and BRF might have played an important role for the  
320 nucleation process of the Le Teil earthquake. Furthermore, the same authors<sup>35</sup>  
321 address the question of the indetermination of the dip angle for the mainshock  
322 (between 40° and 65°). The causal fault system is perhaps more complex than  
323 one single fault (LRF). It is well known that the nucleation process of an earthquake  
324 may occur around the geometrical irregularity of a complex fault system<sup>50-52</sup>. The  
325 steeper BRF (69° dip in our study) may therefore have played a role in both seismic  
326 events, the mainshock and the aftershock.

327

#### 328 4. Conclusion: a hydraulic triggering mechanism

329

330 We developed here two separate numerical models and used a decoupled  
331 modeling approach to compare the potential mechanical and hydraulic triggering  
332 factors for the earthquake of 11 November 2019 at Le Teil (France). The 3D  
333 geometry of the fault system was reconstructed through the surface rupture  
334 evidences of BRF found by our DInSAR interpretation (in addition to LRF) and a  
335 newly processed local seismic cross-section. Using the soil moisture data in the  
336 studied zone during the decade between 2010 and 2019, we carried out hydraulic

337 numerical simulations in the three dimensional volume. The near-vertical BRF  
338 geometry could have serve as major drain of the strong rainfall during the month  
339 before the earthquake, thus increasing the pore pressure at depth so as to possibly  
340 trigger a very shallow earthquake on LRF. The pore pressure at depth becomes a  
341 local peak just before the 2019 Le Teil earthquake at the intersection of the two  
342 segments BRF and LRF, very close to the hypocenter location determined by other  
343 seismological studies<sup>35</sup>. The estimated amplitude is close to 1 MPa, about four  
344 times more important than the normal stress change elastically loaded on the fault  
345 due to the mass removal of the quarry from the ground surface (Figure 8). This  
346 work thus suggests a hydraulic triggering mechanism at shallow depth on a  
347 network of faults under long-term tectonic stress loading. The hydraulic recharge  
348 of similar fault systems may be the scope of future works in order to improve the  
349 local seismic hazard assessment around sensitive areas.

350

## 351 5. Methods

352

353

### 354 *Differential SAR Interferometry (DInSAR)*

355 The displacements are estimated along the sensor's Line of Sight (LOS), which is  
356 the sensor-to-target direction. DInSAR measures the projection of real motion  
357 along the LOS and provides 1D displacement measurements. Those measurements  
358 are relative in space and time: they are spatially related to a reference point, and  
359 temporally to the date of the first available satellite acquisition. Four  
360 interferograms were produced using Sentinel-1 data (Table S1). The processing is  
361 based on the Gamma processing software (<https://gamma-rs.com>). In order to  
362 interpret these interferograms for identifying and quantifying surface ruptures, an  
363 unwrapping additional step is required. For this step, we used the Minimum Cost  
364 Flow (Constantini, 1998) procedure implemented in Gamma. Unwrapped AO59

365 interferogram is shown in Figure 2. The visual examination allows a first estimation  
366 of the LRF rupture location and the positions of the extremities of a candidate for  
367 the BRF rupture (Figure 3). In order to obtain additional candidates we added  
368 positions of faults from the 1:50 000 geological map (see Figure S1). These faults  
369 were imported in the tool for profiles stacking and displacement estimation  
370 included in the Cosi-corr software<sup>53,54</sup>. Lateral profiles are automatically generated  
371 by the software perpendicularly to the fault candidate (20 on LRF and 20 + 3 added  
372 manually on BRF). Our objective is first to validate points on the fault candidate  
373 as reliable observations if significant differential motion between each side of the  
374 profile is observed and then to quantify this motion. In addition, if the "jump" on  
375 the displacement profile is not exactly on the candidate's position this procedure  
376 allows to adjust the position by displacing the candidate accordingly to the jump's  
377 position. Figure S2 illustrates the use of the tool on the south-west of the LRF.  
378 Finally, the obtained points are connected in order to obtain a continuous rupture  
379 trace. This proposed procedure was found to be sensitive enough for interpreting  
380 the initial interferometric information and the results obtained are in fairly good  
381 agreement with ground failure observations (Figure 2). Although it cannot be fully  
382 exhaustive (minor motions could be missed), this provides a good representation  
383 of the positions of the LRF and BRF and a quantification of their surface  
384 displacements have been proposed. Furthermore, some unwrapping issues can  
385 occur close to the ruptures for two main reasons. First, some sectors of the area  
386 have poor coherence because of possible surface changes occurred during the 6  
387 days time-span due to the earthquake itself or due to the presence of locally  
388 vegetated land covers. Secondly, the observed motion on the ruptures is larger  
389 than quarter of wavelength (i.e. 14 mm). One noteworthy point is the fact that  
390 two parallel ruptures introduces a specific unwrapping issue (illustrated in Figure

391 S3). This may have influenced on the location and quantification of the rupture  
392 traces. Complements on the unwrapping issues can be found, for example, in  
393 Hanssen<sup>55</sup> and Raucoules *et al.*<sup>56</sup>. For these reasons, it is important to  
394 compare/validate the interpretation of the interferogram in respect to the prior  
395 knowledge of faults (e.g. ground observations or boreholes). The consequence is  
396 that it introduces an ambiguity on the distribution of the measured slip between  
397 the two faults. This issue may explain the different results provided by Ritz et al.  
398 (2020)<sup>30</sup> using the same Sentinel-1 data (Figure S4). As this ambiguity cannot be  
399 resolved only on the basis of the interferometric information, we use therefore  
400 additional observations (surface ruptures evidences or/and cores of boreholes).

401

402 *Hydraulic simulations by ComPASS using soil moisture data*

403

- 404 • *Soil Moisture (SM30) data at the Berzème station (SMOSMANIA)*

405 The SMOSMANIA network (Soil Moisture Observing System - Meteorological  
406 Automatic Network Integrated Application) is based on the existing automatic  
407 weather station network of Meteo-France. The SMOSMANIA soil moisture data are  
408 freely available on the web site of the International Soil Moisture Network  
409 (<https://ismn.geo.tuwien.ac.at/en/>). The stations form a Mediterranean-Atlantic  
410 transect following the marked climatic gradient between the two coastlines. The  
411 average distance between two neighbouring stations is approximately 40 km which  
412 is consistent with the spatial resolution of remote sensing soil moisture products  
413 (e.g. SMOS). The station at Berzème is located at less than 15 km from Le Teil  
414 (Figure S6). The vegetation on these sites is made up of natural fallow land, cut  
415 once or twice a year. Since April 24, 2015, four soil moisture probes (ThetaProbe  
416 ML3) are installed per station at depths of 5, 10, 20 and 30 cm. The ThetaProbe is

417 a capacitance probe using the dielectric permittivity properties of the soil to  
 418 estimate the volumetric soil moisture content. The data at depth of 30 cm (noted  
 419 SM30) are used in the hydraulic simulations Ref16, Ref20 (Table 1) and Ref6  
 420 (Table S4). The water content or soil moisture content is the quantity of water  
 421 contained in the soil. The normalized water content (or effective saturation  $S_e$ ) is  
 422 depended on the volumetric water content SM30 (raw data), the residual water  
 423 content  $\theta_r$  (about 12% between 2015 and 2019 at the Berzème station) and the  
 424 saturated water content equivalent to porosity  $\omega$  (about 42% at 30 cm at the  
 425 Berzème station):

$$S_e = \frac{(SM30 - \theta_r)}{(\omega - \theta_r)}$$

426

- 427
- 428 • *SMOS Level 3 Surface Soil Moisture (SSM) Products*

429 The first satellite mission to focus primarily on the collection of soil moisture  
 430 data was the European SMOS satellite that was successfully launched on the 2<sup>nd</sup>  
 431 of November 2009 by ESA. The surface soil moisture data acquired by the SMOS  
 432 satellite between 2010 and 2019 are used in the numerical modeling as boundary  
 433 conditions for the whole nodes at the top surface, except for those belonging to  
 434 the Rhône river. We use here the term Surface Soil moisture (SSM) to refer to the  
 435 volumetric soil moisture in the first few centimeters (0–5 cm) of the soil. It must  
 436 also be noted that ascending and descending overpasses are bound to show  
 437 different values of the retrieved parameters that may not be always comparable,  
 438 and they are, thus, retrieved separately. The SMOS Level 3 SSM products are  
 439 downloaded through the website of the Centre Aval de Traitement des Données  
 440 SMOS (CATDS, <https://www.catds.fr>). The data are presented over the Equal-Area  
 441 Scalable Earth (EASE grid 2)<sup>25</sup> with a sampling of about 25 km x 25 km and the  
 442 studied area is included in one grid cell called L2 (Figures 1a and S6). The CATDS

443 provides either a 10-day SSM product (that contains median, minimum and  
 444 maximum values of soil moisture) or a 3-day product. The 3-day products for  
 445 ascending overpasses are used between Mai 2015 and December 2019 (Figure 6)  
 446 and the 10-day aggregated products for descending overpasses are used between  
 447 March 2010 and December 2019 (Figure S6). As the residual water content  $\theta_r$  is  
 448 almost zero for SMOS acquisitions, the normalized water content (or effective  
 449 saturation  $S_e$ ) depends only on the volumetric water content SSM and the porosity  
 450  $\omega$  (about 50% at 5-10 cm in the studied area given by the Harmonized World Soil  
 451 Database):

$$S_e = \frac{SSM}{\omega}$$

452

- 453
- 454 • *Hydraulic parameters (matrix, fault)*

455 The hydraulic parameters in the Barremian / Urgonian limestones are highly  
 456 variable in the host rock, the damaged zone and the core fault<sup>37-40</sup>. In the Urgonian  
 457 carbonates at Russel (<https://lsbb.cnrs.fr/>, about 90 km southeast of Le Teil), the  
 458 observations show the presence of discontinuities (joints, veins, faults and  
 459 stylolites) that influence the hydraulic properties from core to reservoir scale<sup>38</sup>:  
 460 the porosity varies from 1% to 20% and the permeability varies in a range between  
 461  $10^{-17}$  m<sup>2</sup> and  $10^{-11}$  m<sup>2</sup>. These hydraulic parameters are used by the ComPASS  
 462 platform<sup>45,46</sup> (<https://github.com/BRGM/ComPASS>) for the reference cases (Table  
 463 1) and the sensitivity cases (Table S4).

464

- 465 • *ComPASS platform*

466 The ComPASS code is able to handle complex networks of fractures with  
 467 intersecting for non-isothermal compositional multiphase Darcy flows. The so-  
 468 called hybrid dimensional model couples a 2D model in fractures with a 3D model

469 in the matrix. The model is discretized using a fully implicit time integration  
470 combined with the Vertex Approximate Gradient (VAG) finite volume scheme which  
471 adapted to polyhedral meshes and anisotropic heterogeneous media. The fully  
472 coupled systems are assembled and solved in parallel using the Single Program  
473 Multiple Data (SPMD) paradigm with one layer of ghost cells. This strategy allows  
474 for a local assembly of the discrete systems. Simulations can be run on  
475 unstructured meshes including complex networks of fractures with intersecting,  
476 immersed and non-immersed fractures. The fully coupled systems are assembled  
477 and solved in parallel using the PETSc library and can be run on large computing  
478 clusters. An efficient preconditioner is implemented to solve the linear systems at  
479 each time step and each Newton type iteration of the simulation.

480

- 481 • *Mesh, time step, convergence, element number used by ComPASS*

482 The open-source software platform under LGPL license named SALOME  
483 (<http://www.salome-platform.org>) has been used to generate the mesh for the  
484 whole domain, in order to, ultimately, simulate fluid flows in the faulted region  
485 using the ComPASS platform. The platform relies on the MED format, an internal  
486 data model, which describes meshes and fields stored as sequences of Hierarchical  
487 Data Format 5 (HDF5) structures. It also takes distributed meshes into account,  
488 thus facilitating parallel computations. The geological units and faults (Figure 5)  
489 were meshed by a tetrahedral conformal meshing using the SALOME code. The  
490 unstructured mesh is composed of more than 140,000 tetrahedral elements where  
491 the mesh size has been constrained for specific boundary elements (top surface,  
492 faults, intersection of faults). The fault is meshed as a two-dimensional (2D)  
493 surface with triangular elements which are interconnected with the surrounding  
494 matrix using conformal meshing. The finest elements are localized at the fault top

495 (triangles side lengths around 18 m). The top surface of the domain is composed  
496 of triangles with side length of approximately 50 m as well as triangles at the  
497 intersection of faults. Then, the finest tetrahedrons are localized close to the top  
498 surface and around the faults while the mesh becomes coarser by moving away  
499 from faults and the top surface (where triangles have side lengths of more than  
500 250 m). For each simulation and at each time step, the nonlinear system is solved  
501 using a Newton algorithm. The GMRES stopping criterion on the relative residual  
502 is fixed to  $10^{-8}$ . The Newton solver is convergent if the relative residual is lower  
503 than  $10^{-8}$  as well. For each simulation, the initial timestep is about one hour and  
504 the maximum timestep is one day.

505

- 506 • *Hydraulic model and numerical simulations by ComPASS*

507 The model domain is set for a dimension of 5 km by 4 km by 3.5 km. The top  
508 surface of the model corresponds to the elevation of the area. The domain is  
509 composed of the geological units and faults in the studied area (Figure 5). Each  
510 unit and fault is considered homogenous in porosity and permeability (e.g. the  
511 permeability of the Apto-albian geological unit, see table 1). As a preliminary step,  
512 the initial state of the hydraulic system, is achieved by performing a first simulation  
513 over a long period (about 100 years) to reach an equilibrium state in the  
514 unsaturated zone where a diphasic flow "air/water" is simulated. In the initial state,  
515 the whole domain is considered fully saturated with a hydrostatic pressure state.  
516 For the boundary conditions, two different Dirichlet conditions are considered for  
517 the nodes at the top surface. At the nodes which belong to the Rhône river, we fix  
518 a constant pressure (1 bar) and a constant saturation (0 for the gas saturation).  
519 At the other nodes of the top surface, the gas saturation is gradually increased  
520 over time from a fully saturated state until to reach 0.9 (corresponding to a water

521 saturation  $Se$  of 0.1). The “no flow” boundary condition is applied on the four  
522 lateral and bottom boundaries. In the unsaturated zone, the values of relative  
523 permeability are defined by the power law  $K_{rw} = Se^2$  and  $K_{ra} = (1 - Se)^2$  for the  
524 water and air phase, respectively. The capillary pressure function  $P_c$  is given by  
525 the Corey law  $P_c = -b \times \ln(Se)$  with  $b = 2 \times 10^5 Pa$ . This first step gives an initial state  
526 with an unsaturated zone in the upper part of the hydraulic model, at equilibrium  
527 with the Rhône river. In the second step, the effective water saturation  $Se$  is  
528 changed every three (or ten) days during the period between 2010 (or 2015) and  
529 the end of 2019 for all the nodes at the top surface (except for the Rhône river  
530 nodes for which a constant water saturation of 1 is fixed). The variations of the  
531 water saturation, occurring over time, results in pressure variations/pulses in both  
532 unsaturated and saturated zones. More specifically, an increasing of water  
533 saturation at the top of the model, which is related to rainfall events results in  
534 pressure variations from the surface towards greater depth.

535

### 536 *Mechanical simulations by 3DEC<sup>TM</sup>*

537 To model the mechanical effect of mass withdrawal on different faults, we use the  
538 Distinct Element Method of 3DEC<sup>TM</sup> code<sup>49</sup> (Version 5.2, Itasca Consulting Group  
539 Inc.) that explicitly handles discontinuities as mechanically active joints. The model  
540 size is set for a dimension of 19 km by 12 km by 6 km oriented N110°E to be  
541 aligned with principal deformation directions<sup>57</sup>. A limit of the 3DEC<sup>TM</sup> is that  
542 discontinuities are defined only by flat surfaces. Each mechanical fault in the model  
543 corresponds to the mean plane of the geological fault, constraining the geometry  
544 of LRF by the observed fault trace position and a dip of about 50°. We attribute  
545 Coulomb behavior to these faults and their properties given in Table S2 are chosen  
546 according to the values measured for discontinuities in Barremian shale in the

547 French Low Noise Underground Laboratory (<http://lsbb.eu>)<sup>58</sup>. As far as the  
548 lithology is concerned, we extract three layers from the 3D geological model: the  
549 basement, the Upper Jurassic and the Hauterivian layer (Figures 5 and 8). The  
550 discretization using tetrahedral meshes was done directly within the 3DEC<sup>TM</sup>, the  
551 mean edge length is 200 m and the mesh is refined around the ground surface of  
552 mass removal and the target faults using a mean edge length of 100 m (Figure  
553 S7). The model parameters of the porous elastic medium are summarized in Table  
554 S3. In the first step, we realize an initial equilibrium to account for the initial state  
555 consisting of a gravitational loading plus a tectonic loading. We assign stress  
556 boundary conditions to the model (Figure 8a). As there is very few constraints on  
557 stress values, we define a reference model with a maximal horizontal stress of  
558  $\sigma_H = 1.3\sigma_v$  and a minimal horizontal stress of  $\sigma_h = 1.1\sigma_v$  where  $\sigma_v$  is the vertical  
559 principal axis (minimum) defined by confining pressure. The top of the model is at  
560 a reference level corresponding to the lowest point within the area. We apply forces  
561 on top of this model to account for the topography. For the area of the quarry, the  
562 topography is reconstructed from the topography of 1950 (Figure S8) and a  
563 homogeneous additional layer is added corresponding to the volume extracted  
564 between 1833 and 1950. The second step consists in modelling the effect of mass  
565 withdrawal. To do this, the forces on top of the model are relaxed in the area of  
566 the quarry. We have no detailed information on temporal evolution of the  
567 topography, and only two periods are considered for the quarry extraction, before  
568 and after 1950. The volume extracted for the first period 1833-1950 is not well  
569 known and estimated by the quarry owner to be around  $4.8 \times 10^6 \text{ m}^3$ . The area of  
570 the quarry is estimated by using the study of De Novellis *et al.*<sup>34</sup> and the volume  
571 extracted is supposed evenly distributed on the whole surface. The volume  
572 extracted for the second period corresponds to the difference between the

573 topography between 2019 and 1950 over the area of the whole quarry (Figure S8).  
574 Using this observed map, our estimation of this volume is about  $34 \times 10^6 \text{ m}^3$ . The  
575 density of the extracted mass is assumed  $2500 \text{ kg/m}^3$ , corresponding to 12 and  
576 85 million tons for the two periods, respectively. The Coulomb stress change is  
577 given by  $\Delta CFF = |\Delta\tau| - \mu(\Delta\sigma_n - \Delta P)$ , where  $\Delta\tau$  and  $\Delta\sigma_n$  are the shear and normal stress  
578 changes (positive in compression),  $\mu$  the frictional coefficient (Table S2) and  $\Delta P$  the  
579 differential of pressure. The direction of  $\Delta\tau$  is taken to the maximum shear stress  
580 on the given fault geometry. The Coulomb stress change  $\Delta CFF$  related to the mass  
581 withdrawal is estimated from the difference between the two equilibrium steps.  
582 The mass withdrawal generates a relaxing of normal stress on LRF as well as an  
583 increase of shear stress.

584

#### 585 *Seismological data analysis at Clauzel House (CLAU)*

586 The data recorded at Clauzel House (CLAU) are made available to the scientific  
587 community by the quarry owner LAFARGE CEMENTS. The sensor is a three-  
588 component, short-period seismograph (sampling rate at 1056.4 Hz), installed in a  
589 private house to monitor the vibrations due the quarry blasts. The recorded data  
590 of the mainshock include visually unnatural jumps in velocity and this leads to  
591 unexpected level of acceleration. After visiting the station CLAU, we observed that  
592 the station have not been correctly fixed on the house floor and probably may  
593 have been impacted by the fall of miscellaneous objects around. Although the  
594 whole waveform may not be exploitable, the first movement at the beginning of  
595 the signals could be informative<sup>35</sup>. In order to verify the correct polarity, we check  
596 the blast signal of the 25<sup>th</sup> September 2019 for which the origin is known (Ev1 in  
597 Figure 8). For the given records, we remove the linear trend, apply the Butterworth  
598 bandpass filter (order of 8) between 1 and 10 Hz and integrate once using the

599 software SeisGram2K Seismogram Viewer v7.0.0X10 ([www.alomax.net](http://www.alomax.net)) for data  
600 viewing and processing. Then, we exploit the particle motion for a selected time  
601 window manually (Figure S9). We obtain a back azimuth of  $N98^{\circ}E \pm 20^{\circ}$  for the  
602 true value of  $N111^{\circ}E$ . Thus, the particle motion indicates approximatively the  
603 event direction with a margin of error of around  $15^{\circ}$ . We thus use the data from  
604 the same station to estimate the direction of the mainshock of the 11<sup>th</sup> November  
605 2019 and its associated uncertainty.

606

607

#### 608 **Data availability**

609 Acquisitions of Sentinel-1 satellite for DInSAR are provided by the European Space  
610 Agency (ESA, <https://sentinel.esa.int/web/sentinel/sentinel-data-access>). The *in situ* soil  
611 moisture data and SMOS surface soil moisture data are freely available on the web  
612 site of the International Soil Moisture Network (ISMN,  
613 <https://ismn.geo.tuwien.ac.at/en/>) and of the French ground segment for the Level 3  
614 data (CATDS, <https://www.catds.fr/>), respectively. The datasets generated and/or  
615 analyzed in this work are available from the corresponding author on reasonable  
616 request.

617

#### 618 **Code availability**

619 The code that is central to our conclusions is the multiphase flow simulator called  
620 ComPASS. It is an open platform using state of the art numerical schemes to  
621 discretize multiphase Darcian flows on generic unstructured meshes. The version  
622 used is freely available at the GitHub platform (<https://github.com/BRGM/ComPASS>).

623

624

## 625 References

626

- 627 1. Stein, S., Geller, R. J. & Liu, M. Why earthquake hazard maps often fail  
628 and what to do about it. *Tectonophysics* **562–563**, 1–25 (2012).
- 629 2. Klinger, Y., Ji, C., Shen, Z.-K. & Bakun, W. H. Introduction to the Special  
630 Issue on the 2008 Wenchuan, China, Earthquake. *Bulletin of the Seismological*  
631 *Society of America* **100**, 2353–2356 (2010).
- 632 3. Lei, X. Possible roles of the Zipingpu Reservoir in triggering the 2008  
633 Wenchuan earthquake. *Journal of Asian Earth Sciences* **40**, 844–854 (2011).
- 634 4. Kerr Richard A. & Stone Richard. A Human Trigger for the Great Quake of  
635 Sichuan? *Science* **323**, 322–322 (2009).
- 636 5. Deng, K. *et al.* Evidence that the 2008 Mw 7.9 Wenchuan Earthquake  
637 Could Not Have Been Induced by the Zipingpu Reservoir. *Bulletin of the*  
638 *Seismological Society of America* **100**, 2805–2814 (2010).
- 639 6. Gahalaut, K. & Gahalaut, V. K. Effect of the Zipingpu reservoir  
640 impoundment on the occurrence of the 2008 Wenchuan earthquake and local  
641 seismicity. *Geophysical Journal International* **183**, 277–285 (2010).
- 642 7. Ge, S., Liu, M., Lu, N., Godt, J. W. & Luo, G. Did the Zipingpu Reservoir  
643 trigger the 2008 Wenchuan earthquake? *Geophysical Research Letters* **36**,  
644 (2009).
- 645 8. Tao, W., Masterlark, T., Shen, Z.-K. & Ronchin, E. Impoundment of the  
646 Zipingpu reservoir and triggering of the 2008 Mw 7.9 Wenchuan earthquake,  
647 China. *Journal of Geophysical Research: Solid Earth* **120**, 7033–7047 (2015).
- 648 9. Mulargia, F. & Bizzarri, A. Anthropogenic Triggering of Large Earthquakes.  
649 *Scientific Reports* **4**, 6100 (2014).
- 650 10. Gupta, H. K. A review of recent studies of triggered earthquakes by  
651 artificial water reservoirs with special emphasis on earthquakes in Koyna, India.  
652 *Earth-Science Reviews* **58**, 279–310 (2002).
- 653 11. McGarr, A., Simpson, D., Seeber, L. & Lee, W. Case histories of induced  
654 and triggered seismicity. *International Geophysics Series* **81**, 647–664 (2002).
- 655 12. Davies, R., Foulger, G., Bindley, A. & Styles, P. Induced seismicity and  
656 hydraulic fracturing for the recovery of hydrocarbons. *Marine and Petroleum*  
657 *Geology* **45**, 171–185 (2013).
- 658 13. Foulger, G. R., Wilson, M. P., Gluyas, J. G., Julian, B. R. & Davies, R. J.  
659 Global review of human-induced earthquakes. *Earth-Science Reviews* **178**, 438–  
660 514 (2018).
- 661 14. Aochi, H. & Burnol, A. Mechanism of the ML4.0 25 April 2016 earthquake  
662 in southwest of France in the vicinity of the Lacq gas field. *Journal of Seismology*  
663 vol. 22 1139–1155 (2018).
- 664 15. Aochi, H., Le Guenan, T. & Burnol, A. Developing subsurface energy  
665 exploitation strategies by considering seismic risk. *Petroleum Geoscience* vol. 23  
666 298–305 (2016).
- 667 16. Dominique, P., Aochi, H. & Morel, J. Triggered Seismicity in a Flooded  
668 Former Coal Mining Basin (Gardanne Area, France). *Mine Water and the*  
669 *Environment* **41**, 317–334 (2022).
- 670 17. Saar, M. O. & Manga, M. Seismicity induced by seasonal groundwater  
671 recharge at Mt. Hood, Oregon. *Earth and Planetary Science Letters* **214**, 605–  
672 618 (2003).
- 673 18. Heki, K. Snow load and seasonal variation of earthquake occurrence in  
674 Japan. *Earth and Planetary Science Letters* **207**, 159–164 (2003).
- 675 19. Hainzl, S., Kraft, T., Wassermann, J., Igel, H. & Schmedes, E. Evidence for  
676 rainfall-triggered earthquake activity. *Geophysical Research Letters* **33**, (2006).



- 729 37. Cochard, J. *et al.* Reservoir properties of barremian–aptian urgonian  
730 limestones, SE France, Part 1: influence of structural history on porosity-  
731 permeability variations. *Journal of Petroleum Geology* **43**, 75–94 (2020).
- 732 38. Jeanne, P., Guglielmi, Y., Lamarche, J., Cappa, F. & Marié, L. Architectural  
733 characteristics and petrophysical properties evolution of a strike-slip fault zone in  
734 a fractured porous carbonate reservoir. *Journal of Structural Geology* **44**, 93–109  
735 (2012).
- 736 39. Guglielmi, Y., Cappa, F., Avouac, J.-P., Henry, P. & Elsworth, D. Seismicity  
737 triggered by fluid injection - induced aseismic slip. *Science* **348**, 1224–1226  
738 (2015).
- 739 40. Aubert, I., Lamarche, J. & Léonide, P. Ternary fault permeability diagram:  
740 An innovative way to estimate fault zones hydraulics. *Journal of Structural*  
741 *Geology* **147**, 104349 (2021).
- 742 41. Burnol, A. *et al.* Wavelet-based analysis of ground deformation coupling  
743 satellite acquisitions (Sentinel-1, SMOS) and data from shallow and deep wells in  
744 Southwestern France. *Scientific Reports* vol. 9 8812 (2019).
- 745 42. Raucoules, D. *et al.* Validation and intercomparison of Persistent Scatterers  
746 Interferometry: PSIC4 project results. *Journal of Applied Geophysics* **68**, 335–  
747 347 (2009).
- 748 43. Massonnet, D. *et al.* The displacement field of the Landers earthquake  
749 mapped by radar interferometry. *Nature* **364**, 138–142 (1993).
- 750 44. Allanic, C. *et al.* Séisme du Teil (11.11.2019) : structuration géologique 3D  
751 du sous-sol. in *27e édition de la Réunion des Sciences de la Terre* (2021).
- 752 45. Xing, F., Masson, R. & Lopez, S. Parallel numerical modeling of hybrid-  
753 dimensional compositional non-isothermal Darcy flows in fractured porous media.  
754 *Journal of Computational Physics* **345**, 637–664 (2017).
- 755 46. Lopez, S. *et al.* Geothermal Modeling in Complex Geological Systems with  
756 the COMPASS Code. in *Stanford Geothermal Workshop 2018-43rd Workshop on*  
757 *Geothermal Reservoir Engineering* (2018).
- 758 47. El Hajj, M. *et al.* Evaluation of SMOS, SMAP, ASCAT and Sentinel-1 Soil  
759 Moisture Products at Sites in Southwestern France. vol. 10 (2018).
- 760 48. De Novellis, V. *et al.* Author Correction: Coincident locations of rupture  
761 nucleation during the 2019 Le Teil earthquake, France and maximum stress  
762 change from local cement quarrying. *Communications Earth & Environment* **2**, 47  
763 (2021).
- 764 49. Itasca. *3DEC—3 Dimensional Distinct Element Code v5.2.* (Itasca  
765 Consulting Group Inc., 2016).
- 766 50. Yoshida, S. *et al.* Joint Inversion of Near- and Far-field Waveforms and  
767 Geodetic Data for the Rupture Process of the 1995 Kobe Earthquake. *Journal of*  
768 *Physics of the Earth* **44**, 437–454 (1996).
- 769 51. Kaverina, A., Dreger, D. & Price, E. The Combined Inversion of Seismic  
770 and Geodetic Data for the Source Process of the 16 October 1999 Mw 7.1 Hector  
771 Mine, California, Earthquake. *Bulletin of the Seismological Society of America* **92**,  
772 1266–1280 (2002).
- 773 52. Ozacar, A. A. & Beck, S. L. The 2002 Denali Fault and 2001 Kunlun Fault  
774 Earthquakes: Complex Rupture Processes of Two Large Strike-Slip Events.  
775 *Bulletin of the Seismological Society of America* **94**, S278–S292 (2004).
- 776 53. Leprince, S., Ayoub, F., Klingner, Y. & Avouac, J.-P. Co-registration of  
777 optically sensed images and correlation (COSI-Corr): An operational  
778 methodology for ground deformation measurements. in *2007 IEEE international*  
779 *geoscience and remote sensing symposium* 1943–1946 (IEEE, 2007).

- 780 54. Ayoub, F., Leprince, S. & Keene, L. User's guide to COSI-CORR co-  
781 registration of optically sensed images and correlation. *California Institute of*  
782 *Technology: Pasadena, CA, USA* **38**, 49s (2009).
- 783 55. Hanssen, R. F. *Radar interferometry: data interpretation and error*  
784 *analysis*. vol. 2 308 (Springer Science & Business Media, 2001).
- 785 56. Raucoules, D., Colesanti, C. & Carnec, C. Use of SAR interferometry for  
786 detecting and assessing ground subsidence. *Comptes Rendus Geoscience* **339**,  
787 289–302 (2007).
- 788 57. Masson, C., Mazzotti, S., Vernant, P. & Doerflinger, E. Extracting small  
789 deformation beyond individual station precision from dense Global Navigation  
790 Satellite System (GNSS) networks in France and western Europe. *Solid Earth* **10**,  
791 1905–1920 (2019).
- 792 58. Derode, B., Guglielmi, Y., De Barros, L. & Cappa, F. Seismic responses to  
793 fluid pressure perturbations in a slipping fault. *Geophysical Research Letters* **42**,  
794 3197–3203 (2015).
- 795  
796  
797  
798

## 799 **Acknowledgments**

800 This research was conducted as part of a research partnership co-funded by BRGM  
801 and the quarry owner LAFARGE CEMENTS (grants CF19DRP21 and CF21DRP01).  
802 We thank LAFARGE CEMENTS to make available the extracted volumes of rocks  
803 from Le Teil quarry during the period 1850-2019 and the data of the SC03  
804 geotechnical borehole drilled in 2016. A.Bu warmly thanks his former PhD  
805 supervisor Laurent Charlet for the field visit looking for possible water sinkholes  
806 around the epicenter location and the visit of his nearby house at Saint-Thomé  
807 damaged by the earthquake.

808

## 809 **Authors contributions**

810 A.Bu and H.A wrote the main manuscript. A.Bu conceived the hydraulic study,  
811 performed the SMOS and Berzème station data processing and contributed to the  
812 overall interpretation. A.A.L performed the 3D hydraulic model with the ComPASS  
813 version developed by S.L and the post-processing with Paraview with the support  
814 of P.PB. M.F performed the overall SAR data processing with Gamma and D.R  
815 interpreted the unwrapped interferogram. J.M performed the mechanical 3D model  
816 with 3-DEC with the contribution of T.G and contributed with H.A and B.B.S to the  
817 interpretation of the mechanical results. A.Bi and F.P contributed respectively to  
818 the retreatment and interpretation of the seismic M201 profile. C.A performed the  
819 geological data analyses and construct the 3D structural model at regional scale.  
820 M.D, P.D and H.A performed the processing of the signal acquired by the vibration  
821 sensor CLAU. B.B.S conceived the global study. All authors contributed to the text  
822 and reviewed the manuscript.

823

## 824 **Ethics declarations**

825 The authors declare that they have no competing interests as defined by Nature  
826 Research. The research support of LAFARGE CEMENTS to BRGM (grants  
827 CF19DRP21 and CF21DRP01) did not include any role in the conceptualization,  
828 study design, data analysis, decision to publish, or preparation of the manuscript.

829

## 830 **Supplementary information**

831 Suppl\_Info\_V5

832

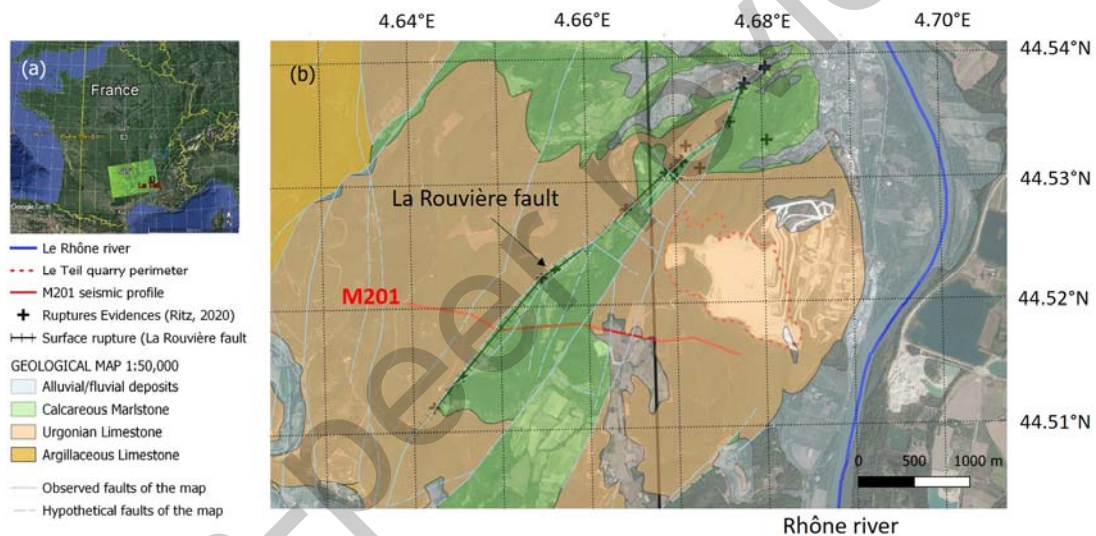
833 Table and Figures

834

835 Table 1 Hydraulic model simulations (parameters and results)

	Ref16	Ref20	Ref21
Soil moisture	SM30 (Berzème, 30 cm depth)	SM30 (Berzème, 30 cm depth)	SSM (SMOS ASC, 3 days)
Matrix Porosity $w_m$	0.2	0.2	0.2
Matrix Permeability $K_m$	$10^{-18} \text{ m}^2$ in Apto-albien $10^{-16} \text{ m}^2$ elsewhere	$10^{-16} \text{ m}^2$	$10^{-18} \text{ m}^2$ in Apto-albien $10^{-16} \text{ m}^2$ elsewhere
Fault Porosity $w_f$	0.1	0.1	0.1
Fault Permeability $K_f$	$10^{-11} \text{ m}^2$	$10^{-11} \text{ m}^2$	$10^{-11} \text{ m}^2$
Fault Width $W$	20 m	20 m	20 m
Maximum differential of pressure ( $\Delta P$ ) along the intersection LRF / BRF	9.82 bar	9.75 bar	9.03 bar

**Figure 1: Map of the studied area.** (a) Location of the studied area near Le Teil city in the southeastern France. Data are combined on Google map, Landsat/Copernicus, SIO, NOAA, US Navy, NGA and GEBCO and include one Copernicus Sentinel image (2019) that contains the 25 km SMOS L2 cell of the EASE equal-area grid (black square). (b) Simplified bedrock geology modified from the BRGM geological map at the 1:50,000 scale (Kerrien *et al.*, 1989) showing the observed faults (light blue solid lines) and hypothetical faults (light blue dashed lines). The surface trace of La Rouvière fault (LRF) (black line) is the black line joining the ruptures evidences (black crosses) of Ritz *et al.* (2020). Also shown the M201 seismic cross-section (solid red line), Le Teil quarry perimeter (dotted red line) and the north-south axis at around 4.67°, which is the boundary between L1 and L2 SMOS cells.



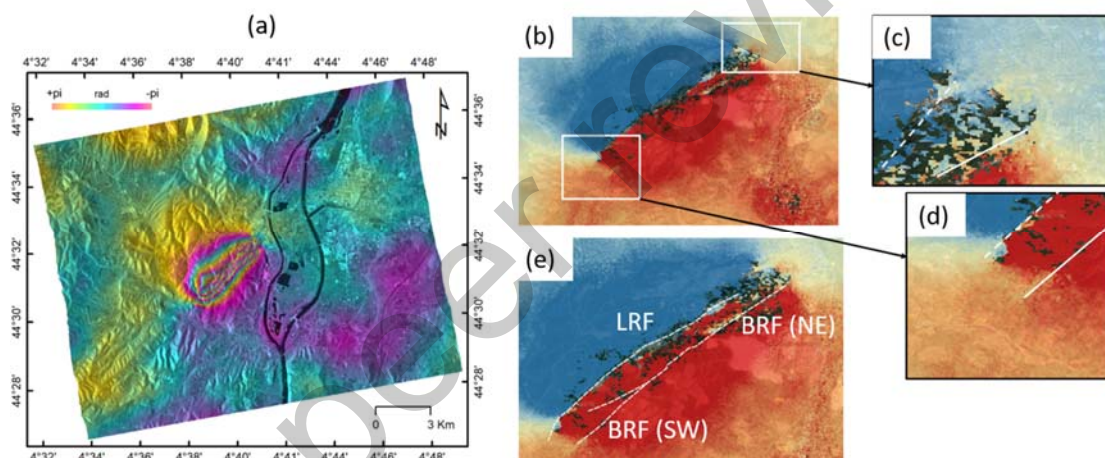
836

837

838

839

**Figure 2. Double surface rupture using Sentinel-1 synthetic-aperture radar data.** (a) A059 (Ascending mode) interferogram (wrapped phase) showing a fringe (phase variation of  $2\pi$ ) corresponding to a surface displacement of 28 mm in line of sight (LOS). The total movement is about 5.5 fringes (about 15 cm in LOS). (b) The unwrapping of A059 allows to convert the phases in LOS displacement of the Sentinel-1 satellite (viewing angle of  $43.7^\circ$ ). The black pixels corresponding to pixels with insufficient coherence and are masked during the unwrapping process. (c)(d) Zooms on both extremities of the detected surface rupture (white lines). (e) Double surface rupture (white lines) of the main fault (La Rouvière; LRF) and the secondary fault (Bayne Rocherenard fault; BRF) including the new position of the North-East part (NE).

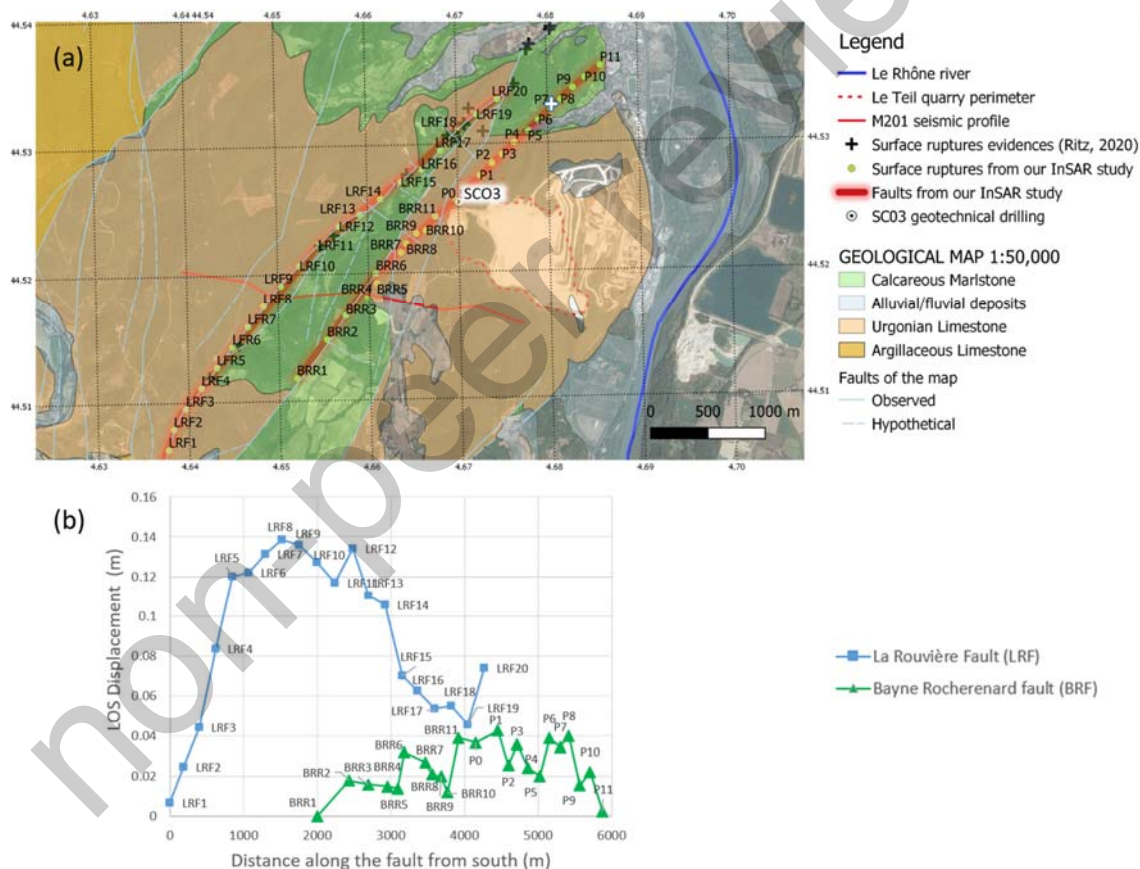


840

841

842

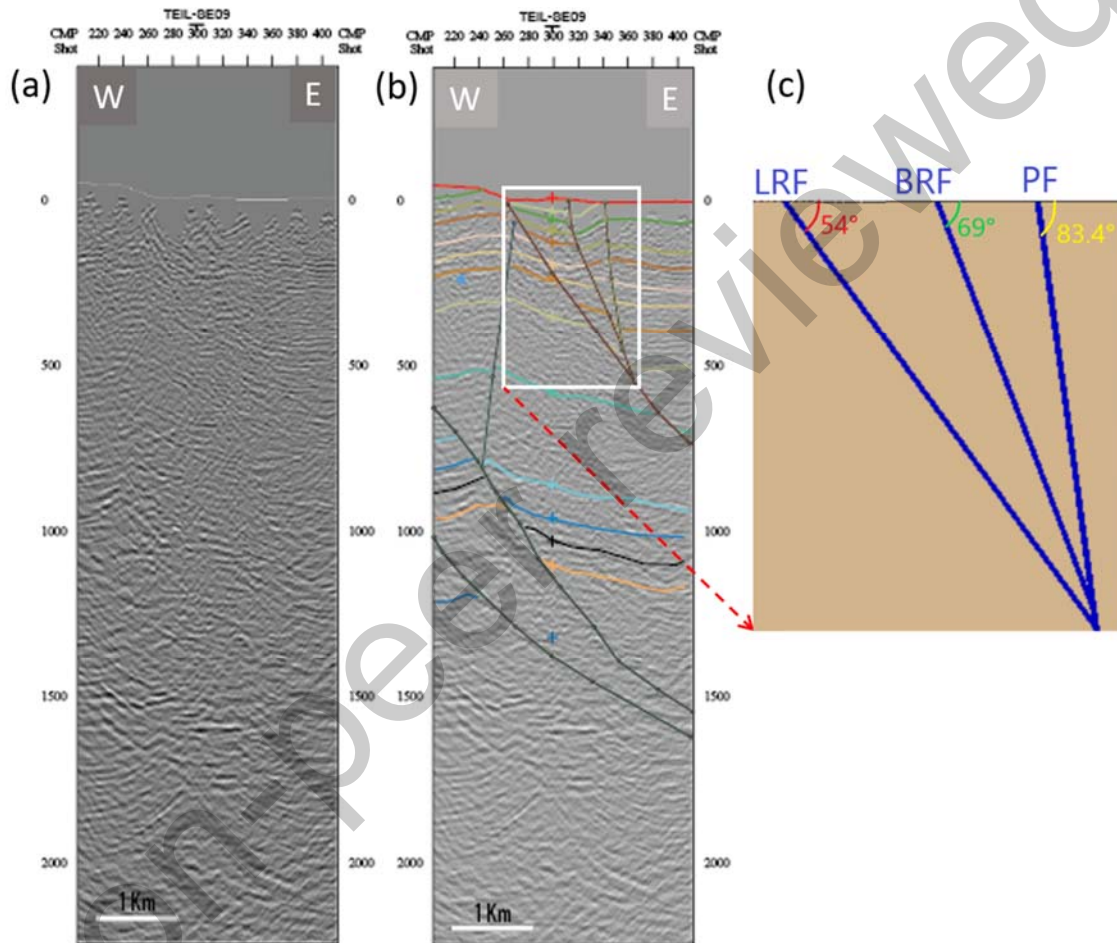
**Figure 3: Distribution of surface displacements along the main and secondary faults. (a) Position of the surface rupture points (yellow circles and red shaded line) and interpretation in terms of fault traces showing two co-seismic rupture lines roughly parallel: the main La Rouvière fault (LRF between LRF1 and LRF20) and the secondary Bayne Rocherenard fault (BRF between BRR1 and BRR11, continuing farther between P0 and P11). Also shown are the previously mapped faults (Kerrien *et al.*, 1989) and the rupture evidences observed by Ritz *et al.* (2020). (b) Comparison of Line of Sight (LOS) displacements for LRF and BRF faults (starting points of both profiles are the most southwestern points LRF1 and BRR1, respectively).**



843

844

845 **Figure 4. Interpretation of the seismic profile M201.** (a) The data along the  
846 cross-section M201 in the time domain (vertical scale is two-way travel time). (b)  
847 Interpretation of the faults and geological layers on M201 consistent with our  
848 updated geological model. (c) True dip angles of LRF (La Rouvière), BRF (Bayne  
849 Rocherenard) and PF (Paurière) faults (see Supplementary information for our  
850 calculation method, texts S1-S3).

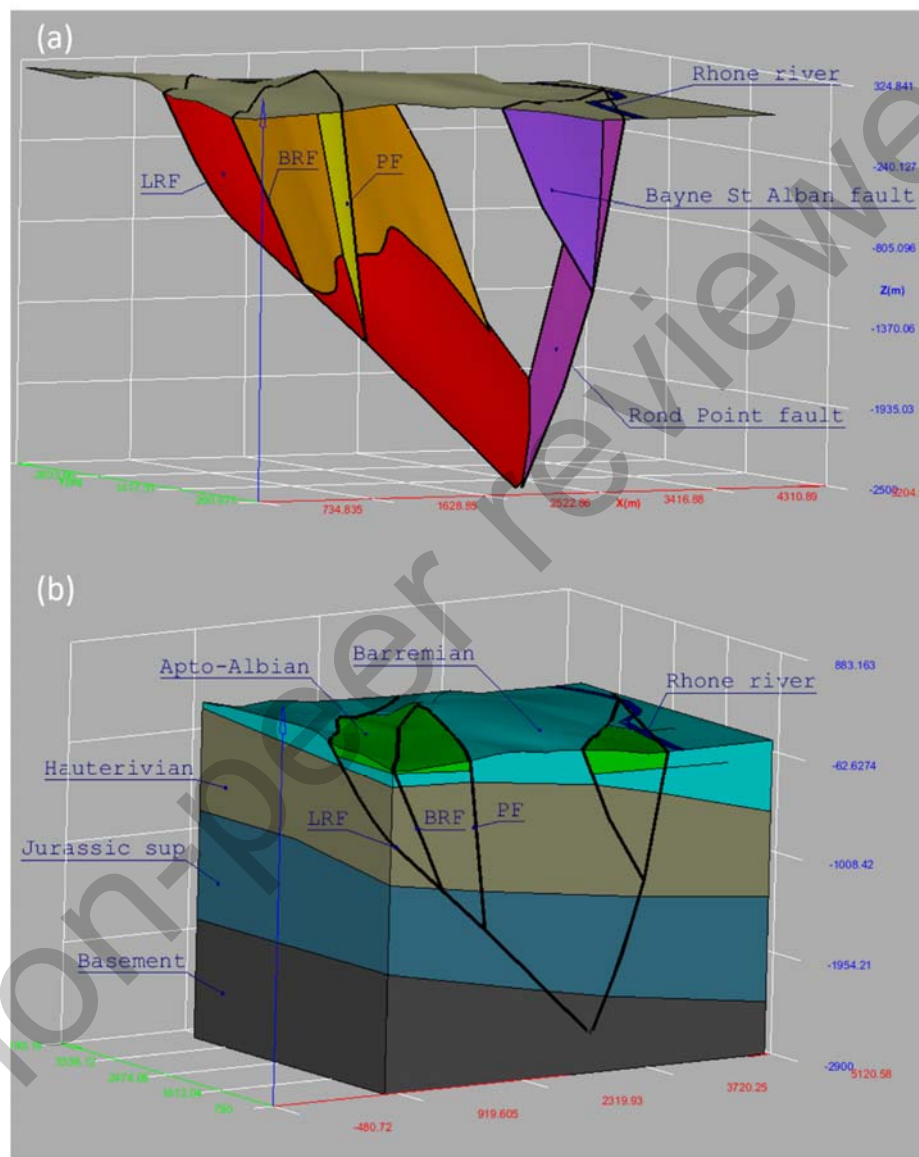


851

852

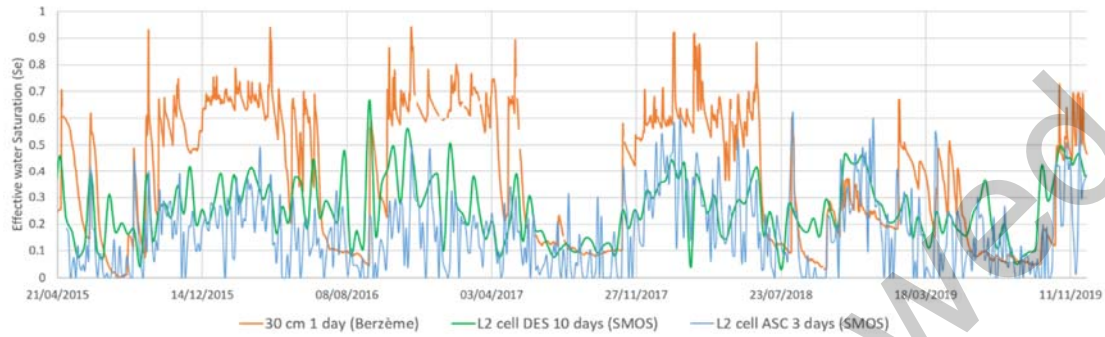
853

854 **Figure 5. Mesh of the hydraulic model. (a)** Three-fault system consisting of  
 855 LRF (La Rouvière), BRF (Bayne Rocherenard) and PF (Paurière) faults. Two other  
 856 faults in the East are also included. Also shown is the topographic surface with the  
 857 Rhône river. (b) Matrix including, among other layers, the surface layer  
 858 characterized by the Apto-Albian clay layer (green) and the Barremian limestones  
 859 (the rest).



860  
861

862 **Figure 6. Surface boundary condition of the hydraulic model.** The effective  
863 saturation  $S_e$  (also called normalized water content) is calculated using *in situ* soil  
864 moisture at 30 cm depth (SM30) at Berzème or Surface Soil Moisture (SSM) every  
865 3 days or 10 days acquired by SMOS in the L2 cell (method section).



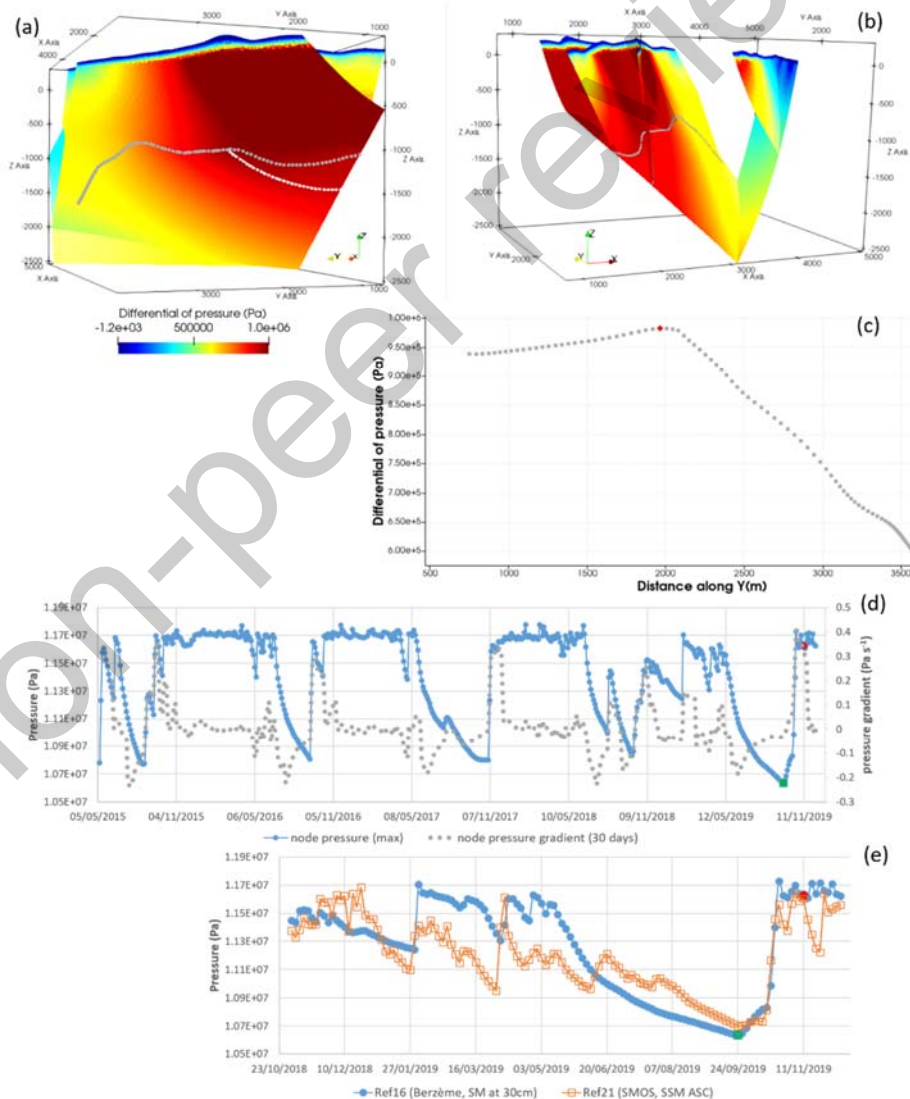
866

867

868

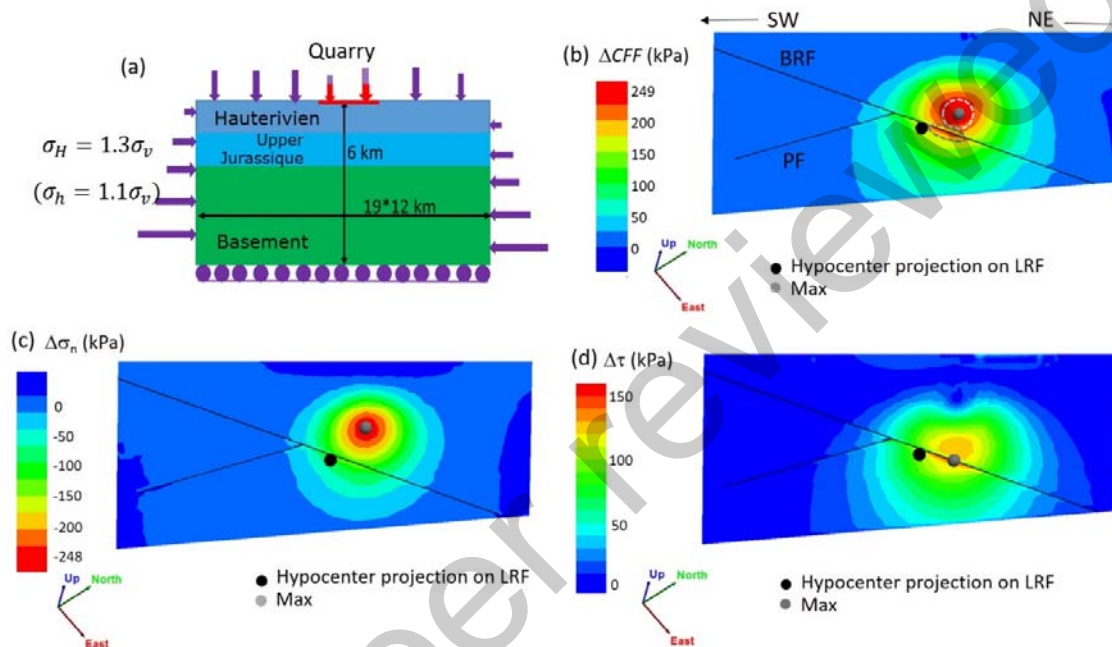
869

870 Figure 7. Simulation result for the reference case using the soil moisture  
 871 at 30 cm (Ref16). (a) Differential of pressure ( $\Delta P$ ) on LRF between 11<sup>th</sup>  
 872 November 2019 and 24<sup>th</sup> September 2019. The intersection of BRF (or PF) with  
 873 LRF is indicated by a grey (or white) dotted line. (b)  $\Delta P$  on the local fault system  
 874 (same view as in Figure 5). (c) Spatial variation of  $\Delta P$  along the intersection line  
 875 between LRF and BRF. Red diamond is the position of the node along this line  
 876 where  $\Delta P$  is maximum. (d) Temporal pressure variation between 2015 and 2019  
 877 at the node where  $\Delta P$  is maximum (blue line) and the pressure gradient for the  
 878 previous 30 days (dotted grey line). The filled green square indicates the relative  
 879 pressure minimum on 24<sup>th</sup> September 2019. The filled red circle indicates the  
 880 pressure on 11<sup>th</sup> November 2019. (e) Zoom of (d) during the year 2019. Also  
 881 shown is the result of the Ref21 case using the surface soil moistures (SSM).



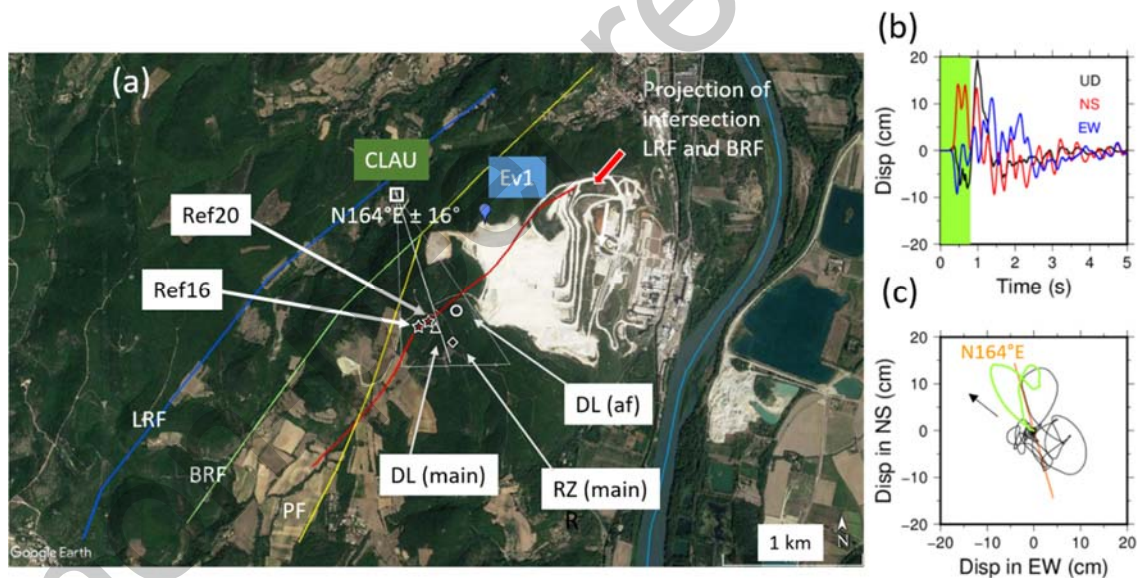
882  
 883

884 **Figure 8. Mechanical simulation by 3DEC™.** (a) Conception of the mechanical  
 885 model (change of the topography is given by a change of force on the ground  
 886 surface). (b) Coulomb stress change ( $\Delta CFF$ ) on LRF related to mass withdrawal.  
 887 Two areas of peak are identified as highlighted by broken lines. (c) Normal stress  
 888 change on LRF. (d) Shear stress change on LRF. Grey point indicates maximum  
 889 stress change. Black point indicates the projection of hypocenter location  
 890 determined by Delouis *et al.* (2021) on LRF.



891  
 892  
 893

894 **Figure 9. Comparison of different epicenter locations of Le Teil**  
 895 **earthquake.** (a) Ref16 and Ref20 (stars) are the locations of maximum  
 896 overpressures calculated by both reference cases Ref16 and Ref20. The red line  
 897 represents the surface projection of the intersection at depth between LRF and  
 898 BRF. Ev1 is the location of the blast event of 25th September 2019 in the quarry  
 899 that is used in the analyses (Method section). DL (main): Epicenter location  
 900 (triangle) of the mainshock suggested by Delouis et al. (2021). RZ (main):  
 901 Epicenter location (losange) suggested by Ritz et al. (2020). DL (af): Epicenter  
 902 location (circle) of the aftershock (MI 2.8) of the 23 November 2019 suggested by  
 903 Delouis et al. (2021). Also shown is the sensor at the private Clauzel house (CLAU)  
 904 located between LRF and BRF. (b) Waveforms in displacement of the earthquake  
 905 event recorded by the sensor CLAU (integrated once from original record in  
 906 velocity). The three components are displayed (NS, EW, UD). (c) Horizontal  
 907 particle motion for the selected time window of the beginning of the signals (shown  
 908 in panel (b) with green color) and associated polarity (orange line).



909

**Supplementary Information to “Double surface rupture and hydraulic recharge of a three-fault system during the Mw 4.9 earthquake of 11 November 2019 at Le Teil (France)”**

André Burnol<sup>1\*</sup>, Antoine Armandine Les Landes<sup>1</sup>, Daniel Raucoules<sup>1</sup>,  
Michael Foumelis<sup>1</sup>, Cécile Allanic<sup>1</sup>, Fabien Paquet<sup>1</sup>, Julie Maury<sup>1</sup>, Hideo  
Aochi<sup>1</sup>, Théophile Guillon<sup>1</sup>, Mickael Delatre<sup>1</sup>, Pascal Dominique<sup>1</sup>, Adnand  
Bitri<sup>1</sup>, Simon Lopez<sup>1</sup>, Philippe P. Pébay<sup>2</sup>, Behrooz Bazargan-Sabet<sup>1</sup>

1. BRGM, 3 avenue Claude Guillemin, BP 36009, 45000 Orléans, France

2. Eredio, 28 rue de la Plane, 84330 Le Barroux

\*Corresponding Author.

Email: [a.burnol@brgm.fr](mailto:a.burnol@brgm.fr)

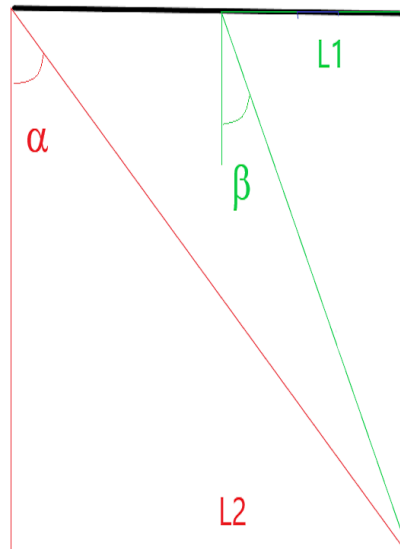
This file contains:

*Texts S1-S3,*

*Tables S1-S4,*

*Figures S1-S9.*

Text S1: Geometry of a two-fault system using a seismic profile.



The Two-way travelttime (TWT) result of a seismic profile is often not adequate to measure the true dip angle of one single fault due to the variations of the velocity with depth. If the lateral velocity variations are small compared to the variations with depth, we can use the ratio of apparent dip angles of a two-fault system in order to calculate both true dip angles.

Alpha ( $\alpha$ ) and Beta ( $\beta$ ) are the supposed constant deviation to the vertical of La Rouvière fault (LRF) and Bayne Rocherenard fault (BRF), respectively.

L1 (and L2) is the horizontal distance between the projection of the intersection point of both faults and the intersection of LRF (and BRF) with the ground surface.

There is a simple trigonometric relationship between these four parameters:

$$\frac{\tan \beta}{\tan \alpha} = \frac{L1}{L2} \quad (1)$$

The equation to solve is therefore:

$$\frac{\tan x}{\tan \mu * x} = \lambda \quad (2)$$

With :

- the unknown x that is the deviation to vertical of BRF
- mu ( $\mu$ ) the ratio between alpha and beta
- lambda ( $\lambda$ ) the ratio between L1 and L2

We develop a python program using the Newton algorithm to resolve this equation for a couple of values ( $\mu$ ,  $\lambda$ ) given by the seismic M201 profile (see Figure 4).

If  $\mu = 4$ , there is an explicit solution:

$$(\tan x)^2 = 3 - 2\lambda - 2\sqrt{1 + (\lambda - 1)^2} \quad (3)$$

If  $\mu$  value is less than 4, the Newton method is applied using a first estimate corresponding to the explicit solution obtained with  $\mu = 4$  (see text S2).

## Text S2: Python script to resolve the equation (2)

```
#!/usr/bin/env python3

"""
:author: André Burnol
:date: 08 avril 2021
"""

from math import tan, atan, cos, sqrt, pi

def beta4rad(l):
    """fonction inverse de  $l = \tan(x)/\tan(4x)$ 

    x=0 if l=1/4
    """
    return atan(sqrt(3 - 2 * l - 2 * sqrt(l**2 - 2 * l + 2)))

def beta4(l):
    """fonction inverse de  $l = \tan(x)/\tan(4x)$ 

    x=0 if l=1/4
    """
    return 180 * beta4rad(l) / pi

def betarad_from_mu_lambda(mu, l):
    """fonction inverse de  $l = \tan(x)/\tan(\mu * x)$ 

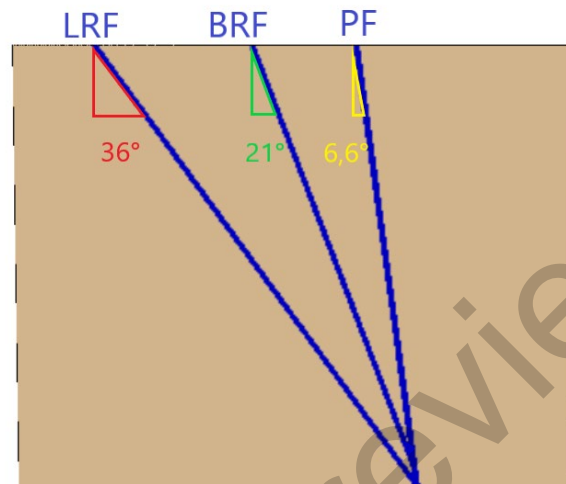
    x=0 if l=1/mu
    """
    x0 = 4/mu * beta4rad(mu * l/4)
    x = x0
    epsilon = 1e-14 # objectif en erreur relative
    delta = - (tan(x)-l*tan(mu*x))/(1/cos(x)**2-mu*l/cos(mu*x)**2)
    while abs(delta) > epsilon * abs(x):
        x = x + delta
        # méthode de Newton pour résoudre  $\tan(x) - l * \tan(\mu*x) = 0$ 
        delta = - (tan(x)-l*tan(mu*x))/(1/cos(x)**2- mu*l/cos(mu*x)**2)
    return x

def beta_from_mu_lambda(mu, l):
    """fonction inverse de  $l = \tan(x)/\tan(\mu*x)$ 

    if lambda=l=0.5128 and mu=1.76
    >>> beta_from_mu_lambda(1.76, 0.5128)
    20.55150781493907
    >>> beta_from_mu_lambda(1.76, 0.5128)*1.76
    36.170653754292765
    >>> beta_from_mu_lambda(1.76, 0.5128)/3.1
    6.629518649980345
    """
    return 180 * betarad_from_mu_lambda(mu, l) / pi
```

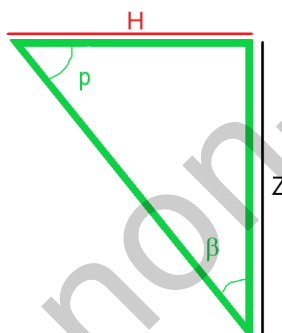
*Text S3: Application to the three-fault system using M201 seismic profile and comparison with the observations of SC03 geotechnical drilling*

From the M201 seismic profile (see Figure 4), we found  $(\mu, \lambda) = (1.76, 0.5128)$  and the solution given by the  $\beta_{\text{from\_mu\_lambda}}(\mu, \lambda)$  is  $\beta = 21^\circ$  and therefore  $\alpha = \mu * \beta = 36^\circ$ . The same method is used for the Paurière fault (PF), we found using M201 profile a ratio of both angles of  $\mu_2 = 3.1$  and therefore the deviation of PF to the vertical is  $\beta / 3.1 = 6.6^\circ$ .

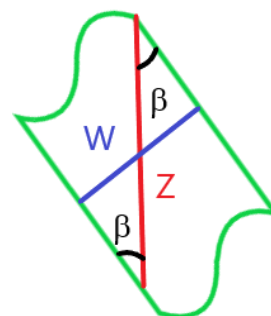


The corresponding dip angles of LRF, BRF and PF are therefore  $54^\circ$ ,  $69^\circ$  and  $83.4^\circ$  (Figure 4c).

Another way to calculate the deviation to the vertical of BRF is to use the observations of SC03 geotechnical drilling conducted in 2016 by the quarry owner (see Figure S5 below):



$$\tan \beta = \frac{H}{Z} \quad (4)$$



$$Z \times \sin \beta = W \quad (5)$$

In Figure S5, the photo S5b of SC03 core reveals a natural sub-vertical fracture at 90.5m vertical depth (with calcite veins). By using  $(H,Z) = (35.6 \text{ m}, 90,5 \text{ m})$ , we found  $\beta = 21.47^\circ$  using (4). Both values of the dip angle of BRF we found are therefore consistent and credible if it assumed that this dip angle is laterally and vertically constant. Using this  $\beta$  value, we can estimate the thickness of BRF noted  $W$  by supposing that the height  $Z$  of (5) is located between a depth of approximately 83 m to 115 m (see Figure S5):  $W = 32 \text{ m} * \sin (21.47^\circ) = 11.7 \text{ m}$ . Therefore, a range of values of the width between 10 m and 30 m can be used (see Tables 1 and S4).

- **Supplementary tables**

*Table S1: Characteristics of the produced interferograms.*

Track ID	Acquisition dates	Perpendicular baseline (m)	Time span (days)
059 (ascending)	6/11/2019 and 12/11/2019	13	6
161 (ascending)	7/11/2019 and 13/11/2019	92	6
037 (descending)	11/11/2019 and 17/11/2019	7	6
139 (descending)	6/11/2019 and 12/11/2019	51	6

*Table S2: fault parameters after Derode et al (2015) used for 3DEC<sup>TM</sup> simulation.*

Parameters	Values
Normal stiffness $k_n$ [GPa/m]	20
Shear stiffness $k_s$ [GPa/m]	20
Friction coefficient $\mu$	0.6

*Table S1 : Model parameters of the medium for 3DEC<sup>TM</sup> simulation. Thickness represent the value below le Teil. Each layer is inclined slightly of 3° to 5°.*

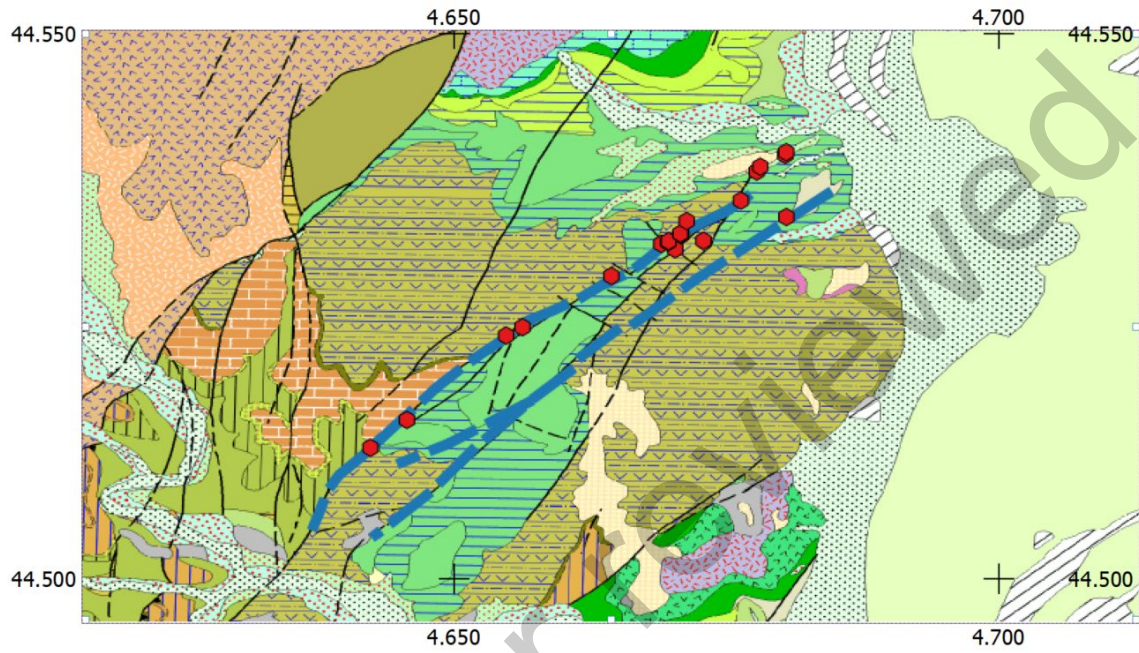
Parameters	Value		
	Hauterivian	Upper Jurassic	Basement
Poisson ratio $\nu$	0.24	0.27	0.3
Young modulus E [GPa]	42	16	61
Density [kg/m <sup>3</sup> ]	2500	2600	2690
Thickness [m]	420	780	-

Table S4: ComPASS results for a 10-fold decrease of the fault permeability and fault porosity compared to the reference cases (Table 1).

	Ref6	Ref19
Soil moisture	SM30 (Berzème, 30 cm depth)	SSM (SMOS DES, 10 days)
Matrix Porosity $w_m$	0.2	0.2
Matrix Permeability $K_m$	$10^{-18} \text{ m}^2$ in Apto-albien	$10^{-18} \text{ m}^2$ in Apto-albien
	$10^{-16} \text{ m}^2$ elsewhere	$10^{-16} \text{ m}^2$ elsewhere
Fault Porosity $w_f$	0.01	0.01
Fault Permeability $K_f$	$10^{-12} \text{ m}^2$	$10^{-12} \text{ m}^2$
Fault Width $W$	20 m	20 m
Maximum differential of pressure ( $\Delta P$ ) along the intersection LRF / BRF	9.6 bar	7.3 bar

- **Supplementary Figures**

*Figure S1:* position of our interpretation of the A059 interferogram on the 1:50 000 geological map (Kerrien et al., 1989). Black lines (solid and dotted): the position of the faults resulting from the geological map. Blue lines: our rupture lines based on the DInSAR results. Red dots: the observations of surface ruptures from Ritz et al. (2020).



*Figure S2:* example of use of the Cosi-corr's profiles stacking tool. Left: interferogram A059 as represented in Cosicorr: red line fault "candidate" for LRF, yellow area containing the 10 profiles to be stacked (1500m X 150m). Right: stacked profile across LRF (position in pixels – i.e. 15m – displacement values in meters). Displacement on the fault is automatically computed as the difference at 0 position between the 2 green lines (linearly fitting the motion each side of the fault).

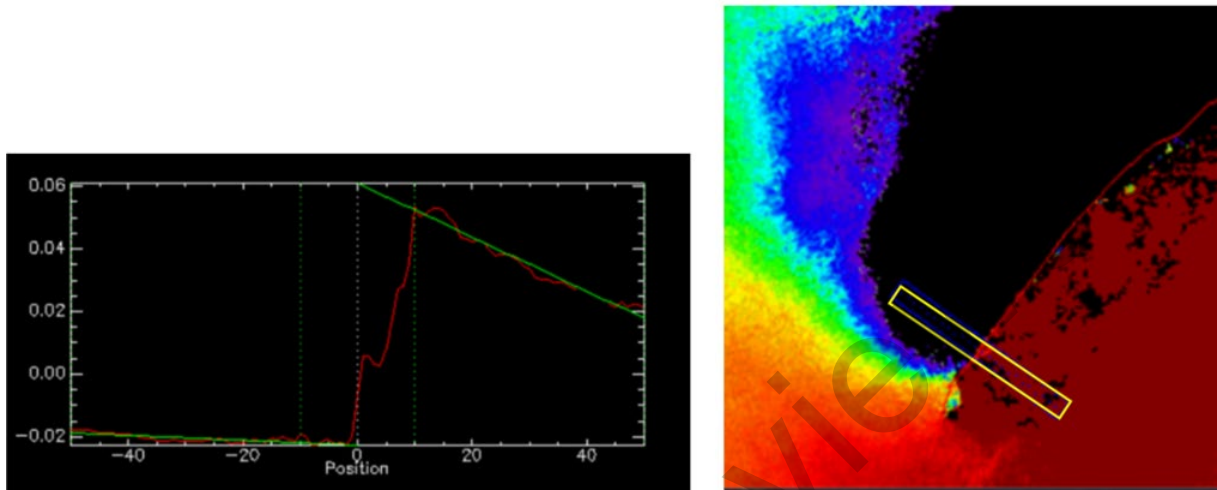
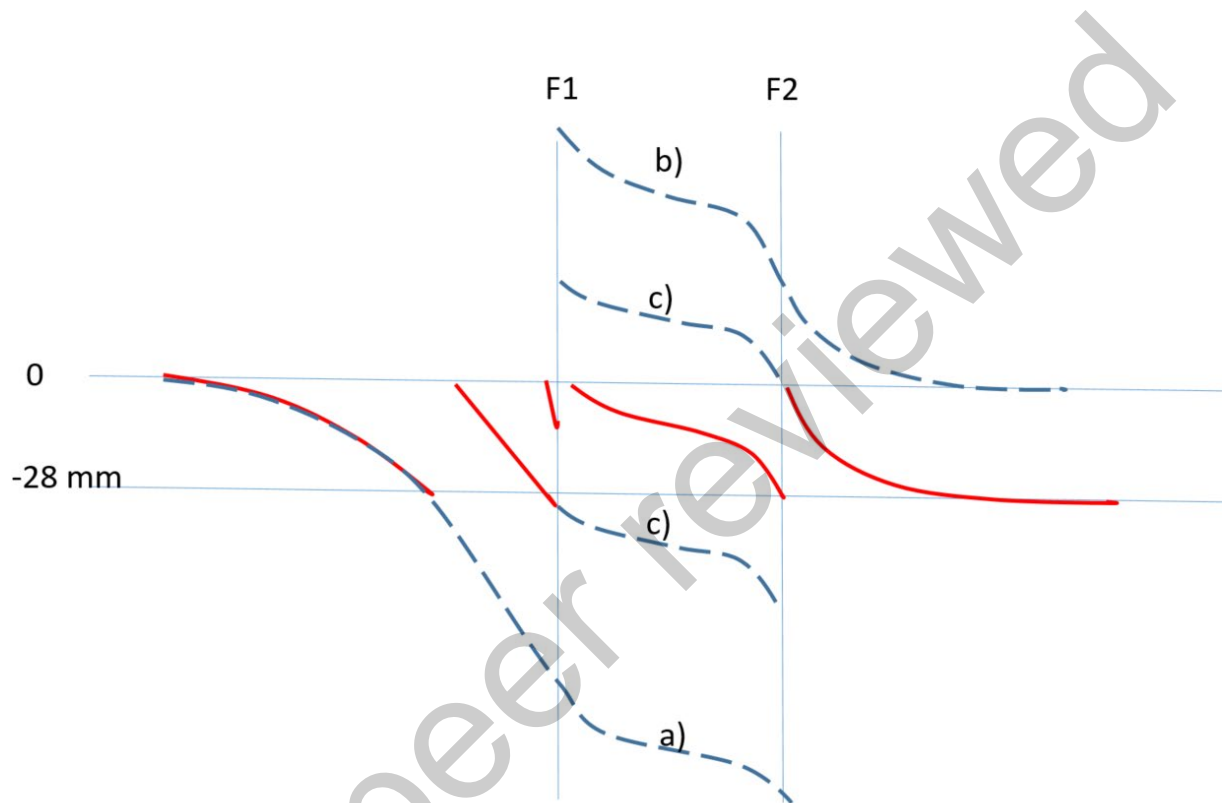


Figure S3: Diagram illustrating (in a very simplified way) a specific unwrapping issue due to two parallel jumps (in our case two surface ruptures represented by F1 and F2). Red line is a profile on the original wrapped interferogram. Assuming that the displacement should be zero at  $\pm\infty$  left part of F1 and right part of F2 can be unambiguously unwrapped (blue dashed line). However between F1 and F2 the unwrapping solution results ambiguous: on solution a) all the displacement is on F2, on solution b) all the displacement is on F1, intermediary solutions are possible (e.g. c))



*Figure S4:* comparison of our unwrapped interferogram (A) with the figure (B) adapted from Ritz et al. (2020) on the North-East sector of the area of interest. We can observe that the unwrapping algorithms have distributed differently the slips between the two ruptures. For instance in Ritz et al. (2020) the LRF is locally locked suggesting a more complex behavior than in our interpretation (where this lock is not significant).

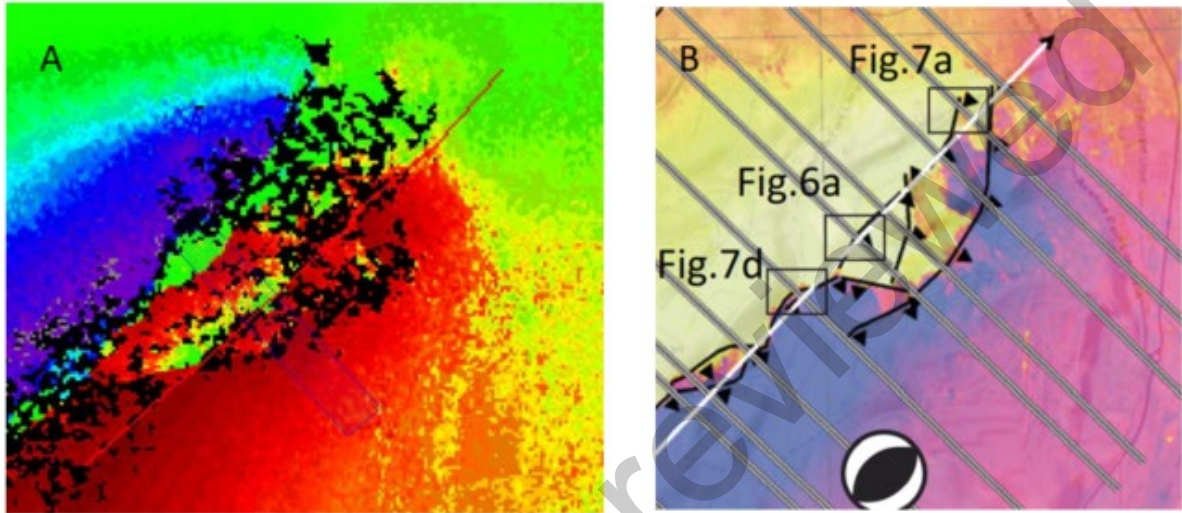
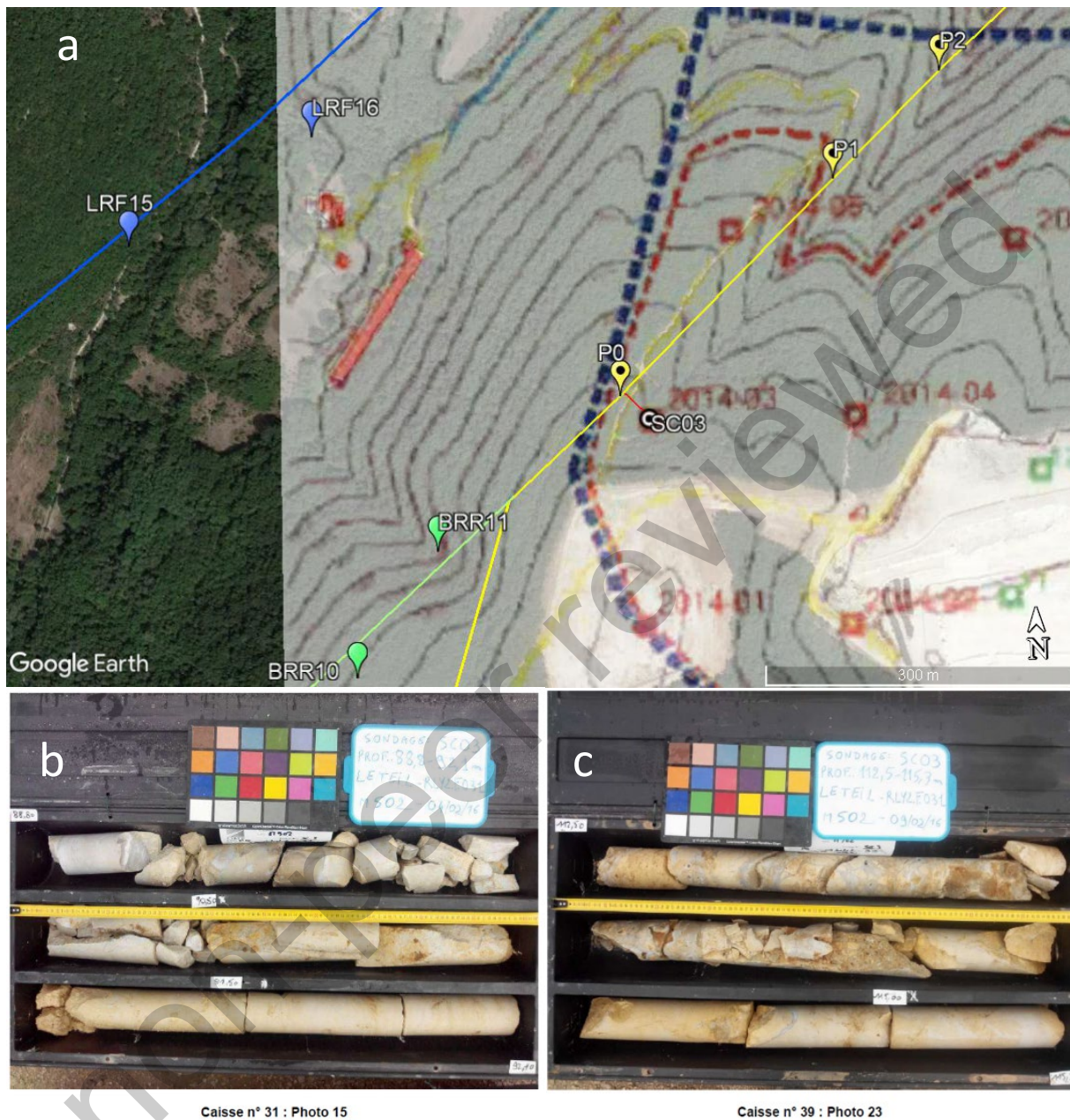
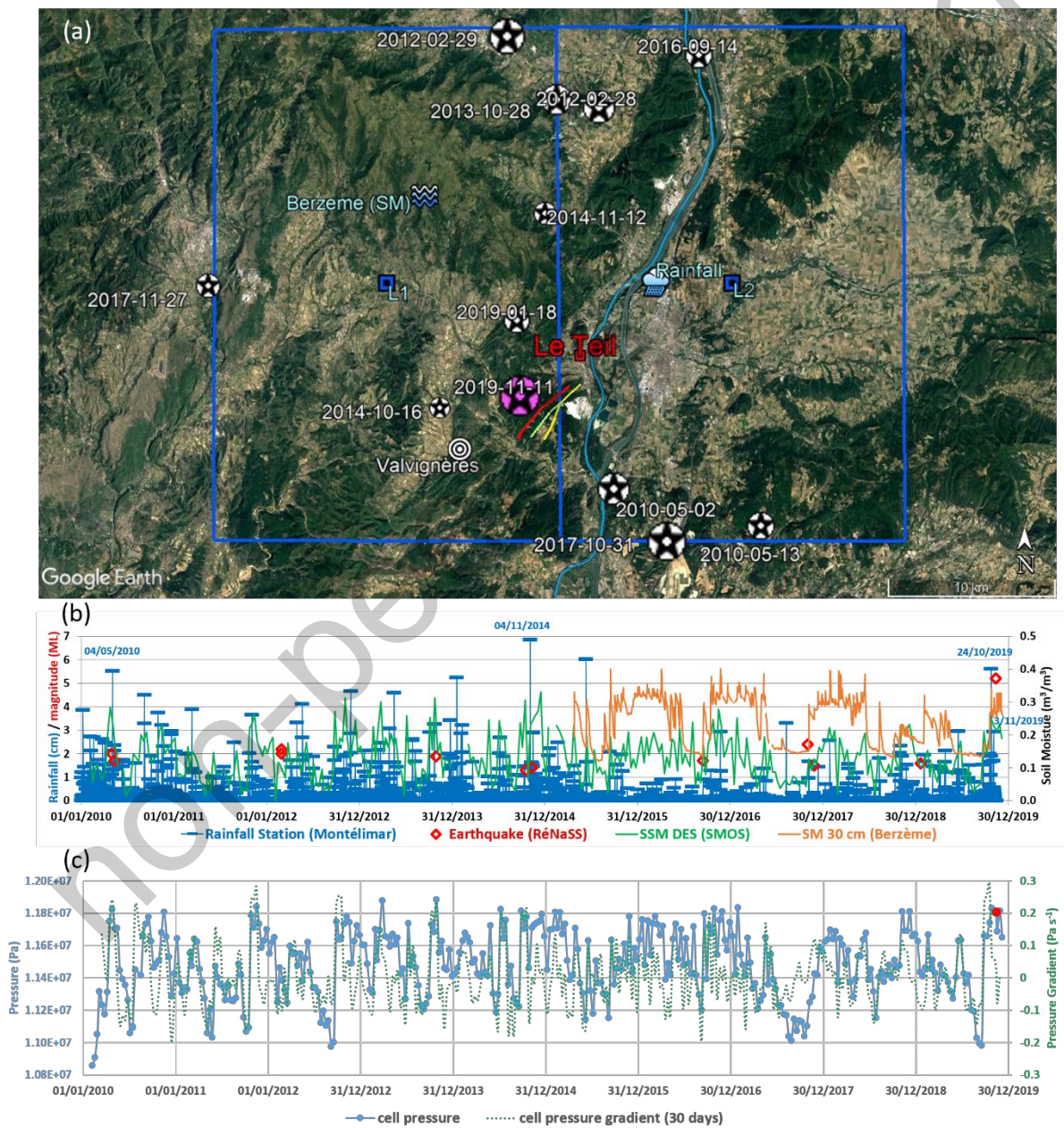


Figure S5: SC03 geotechnical drilling conducted in 2016 by the quarry owner: a) location of SC03 about 35.6 m (red line) southeast of Bayne Rocherenard fault (yellow line near P0) b) core samples at depth between 89 m and 92 m, c) core samples at depth between 112.5 m and 115.3 m.



**Figure S6:** (a) Regional setting with both SMOS cells L1 and L2 around Le Teil. The rainfall station is located in L2, the soil moisture station (Berzème) from the SMOSMANIA network in L1 and the Valvignères borehole in L1. The location and the date of all the seismic events in the area of 50 km x 25 km (L1 and L2) recorded by the French national catalogue (RénaSS) are shown during the 2010-2019 period. (b) Comparison of the rainfall data with the Soil Moisture (SM) at Berzème (1 day) and the Surface Soil Moisture (SSM) acquired by SMOS (descending path, 10 days) during the 2010-2019 period. (c) Cell pressure (blue line) and cell pressure gradient (dotted green line) in the Ref19 case (Table S4) using the Surface Soil Moisture (SSM) acquired by SMOS (descending path, 10 days) during the period 2010-2019.



*Figure S7:* Fault models and numerical meshes in 3DEC simulations. The dimension (x,y,z) is 19 km (N110°E) x 12 km (N20°E) x 6 km (vertical). (a) Fault elements implemented in simulation. (2) A snapshot of simulation in a fault system with respect to the surface quarry. The color indicates the  $\Delta CFF$ , whose color scale is indicative.

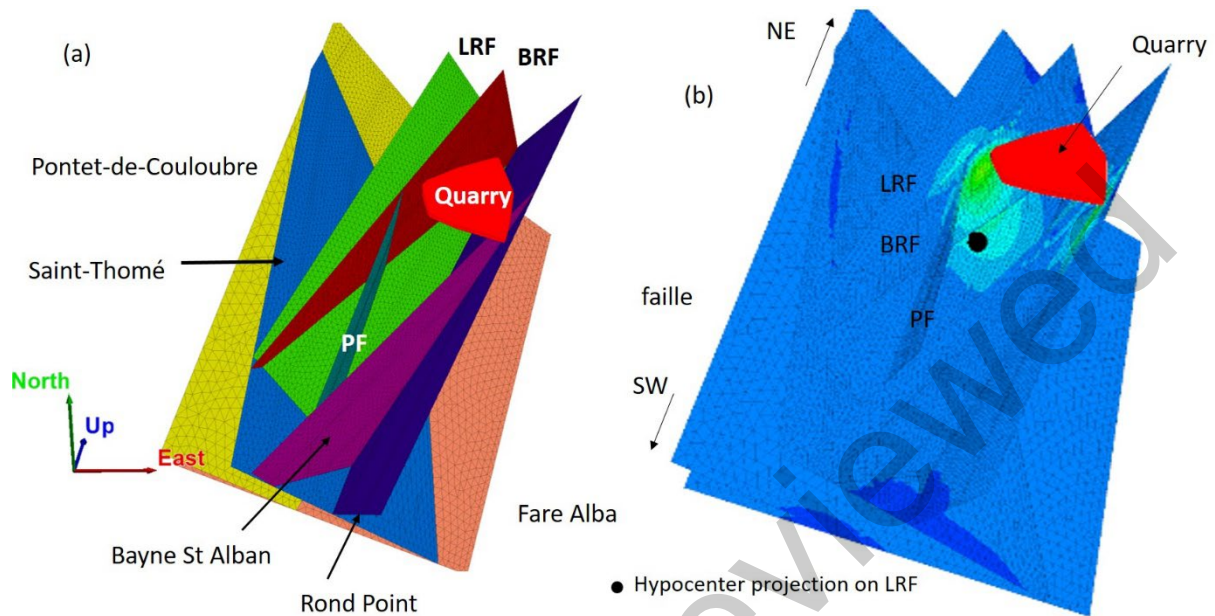


Figure S8: Estimated extracted area and topography change between 1833-2019. The earlier period before 1950 is based on the estimation of De Novellis et al. (2020) and the extracted volume is evenly distributed on the corresponding surface. The extracted volume during the second period after 1950 is estimated from the topography change observed on map.

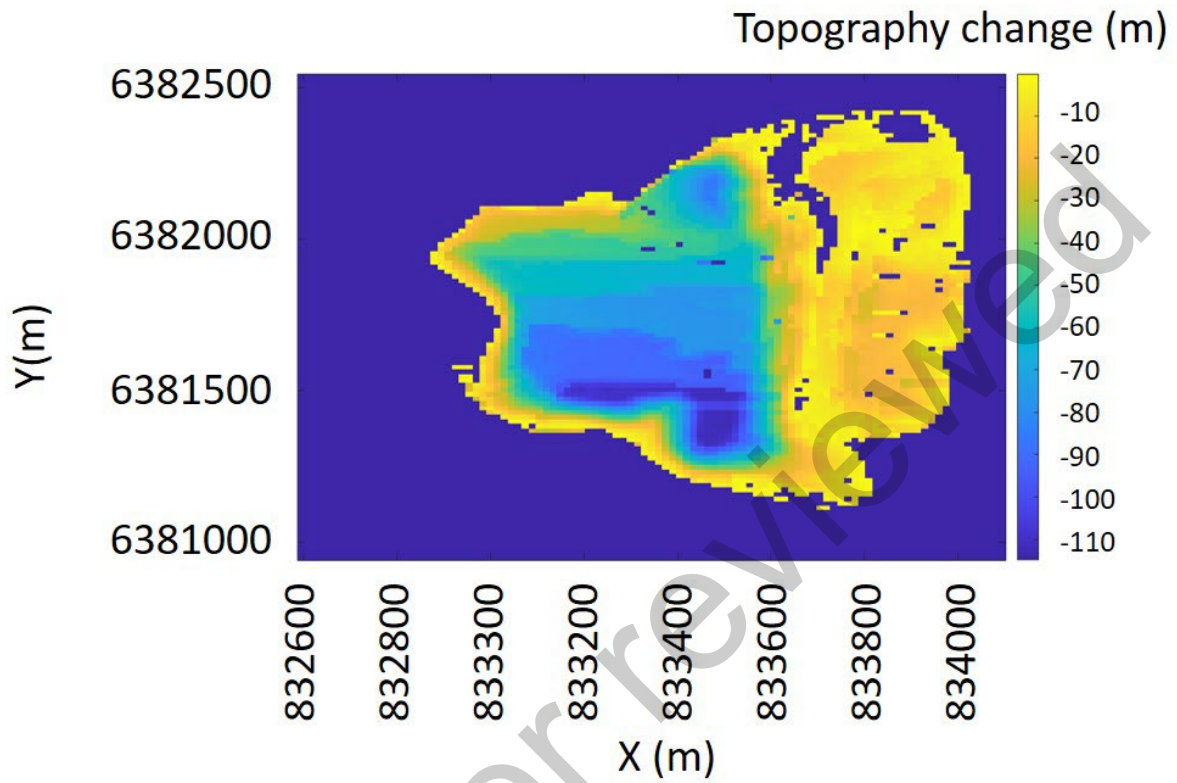
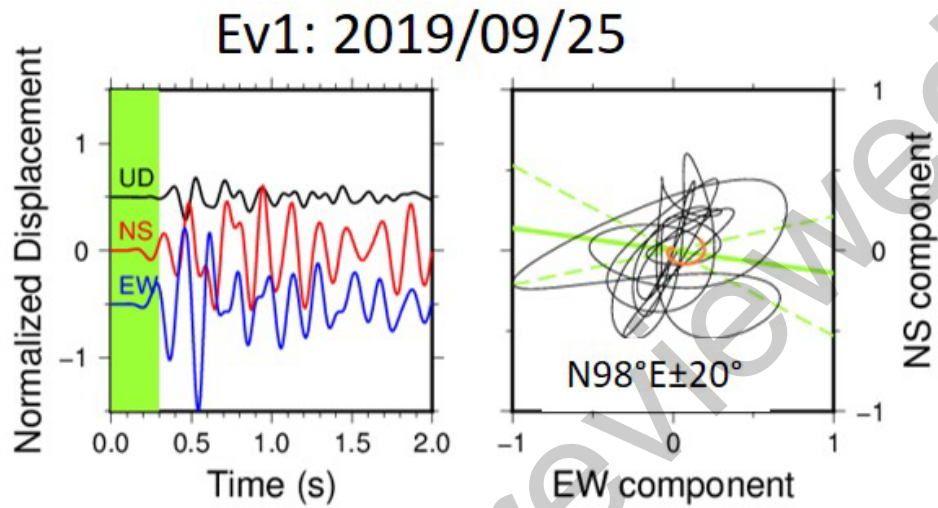


Figure S9: Ground motion recorded at Clauzel house (CLAU) for the blast event of the 25<sup>th</sup> September 2019. Filtered (1-10 Hz) and integrated seismograms in the left panel. The horizontal particle motion at the right. The first 0.3 second is highlighted as red line. The azimuth is estimated to  $N98^{\circ}E \pm 20^{\circ}$  (green line with broken lines) with respect to the true value of  $N111^{\circ}E$ .



- **References**

Derode, Benoit, Yves Guglielmi, Louis De Barros, et Frédéric Cappa. « Seismic responses to fluid pressure perturbations in a slipping fault ». *Geophysical Research Letters* 42, n° 9 (16 mai 2015): 3197-3203. <https://doi.org/10.1002/2015GL063671>.

Y Kerrien, S Elmi, R. Busnardo, G. Camus, G. Kieffer, J. Moinereau, A. Weisbrod. « Carte géol. France (1/50000), feuille Aubenas (865). BRGM : Orléans. Notice explicative par S. Elmi, R. Busnardo, B. Clavel, G. Camus, G. Kieffer, P. Bérard, B. Michaëly (1996), 170 p. » Orléans: BRGM, 1989.

Ritz, Jean-François, Stéphane Baize, Matthieu Ferry, Christophe Larroque, Laurence Audin, Bertrand Delouis, et Emmanuel Mathot. « Surface rupture and shallow fault reactivation during the 2019 Mw 4.9 Le Teil earthquake, France ». *Communications Earth & Environment* 1, n° 1 (27 août 2020): 10. <https://doi.org/10.1038/s43247-020-0012-z>.

De Novellis, Vincenzo, Vincenzo Convertito, Sotiris Valkaniotis, Francesco Casu, Riccardo Lanari, Mario Fernando Monterroso Tobar, et Nicola Alessandro Pino. « Coincident locations of rupture nucleation during the 2019 Le Teil earthquake, France and maximum stress change from local cement quarrying ». *Communications Earth & Environment* 1, n° 1 (18 septembre 2020): 20. <https://doi.org/10.1038/s43247-020-00021-6>.

non-peer reviewed